

Earth Flyby Orbit Determination Project

Giovanni Fereoli

May 1, 2025

Contents

1	Introduction	2
2	Flyby Scenario	2
2.1	Dynamics Model	2
2.2	Measurement Model	2
3	Problem 2: Estimation with Known Models	4
3.1	Filter Setup	4
3.2	Goodness-of-Fit Assessment via Reduced Chi-Square Statistic	4
3.3	Results	5
4	Problem 3: Estimation with Unknown Errors	8
4.1	Filter Setup and Strategy	8
4.2	Preliminary Residual and Trajectory Inspection	9
4.2.1	Impulsive Burn Modeling	10
4.2.2	Process Noise Modeling	11
4.2.3	Note on Propagation to the B-plane	13
4.3	Results	13
4.3.1	<i>OD03</i> : LKF+RTS Filtering with DMC on First 75% of the Arc	13
4.3.2	<i>OD02</i> : LKF+RTS Filtering with SNC and Maneuver Modeling	18
4.3.3	<i>OD01</i> : LKF+RTS Filtering with DMC and Maneuver Modeling	20
4.3.4	<i>OD04</i> : SRIF Filtering with SNC and Maneuver Modeling	22
4.3.5	<i>OD05</i> : LKF+RTS Filtering with DMC on 100% of the Arc	23
4.4	Selection of Final Solution	24
5	Additional Analysis	26
5.1	Comparison with Alternative Filters	26
5.2	B-plane Sensitivity to Mapping Radius	27
5.3	Lessons Learned for Real-World Orbit Determination	28
5.4	Ephemeris Errors	28

1 Introduction

This project addresses the orbit determination (OD) of a spacecraft during an Earth Gravity Assist (EGA) by processing Deep Space Network (DSN) range and range-rate observations. The goal is to estimate the spacecraft state and covariance using filtering techniques across two scenarios: one with accurate models, and one with unknown modeling errors requiring identification and mitigation.

The estimation is performed in an Earth-centered inertial (ECI) frame considering Earth's gravity, solar third-body perturbations, and solar radiation pressure via a cannonball model. Pre-fit and post-fit residuals are evaluated to assess filter performance. Additional analyses include alternative filter strategies and B-plane uncertainty mapping, providing insight into practical challenges in real-world orbit determination.

2 Flyby Scenario

The dynamical models, measurement models, and filtering techniques implemented in this analysis follow the formulations presented in *Statistical Orbit Determination* (Tapley, Schutz, and Born, 2004). Ephemerides for the Earth and Sun are computed following the methodology outlined in *Astronomical Algorithms* (Meeus, 1991). B-plane targeting and coordinate definitions are based on the formalism introduced in *Method of Describing Miss Distances for Lunar and Interplanetary Trajectories* (Kizner, 1961).

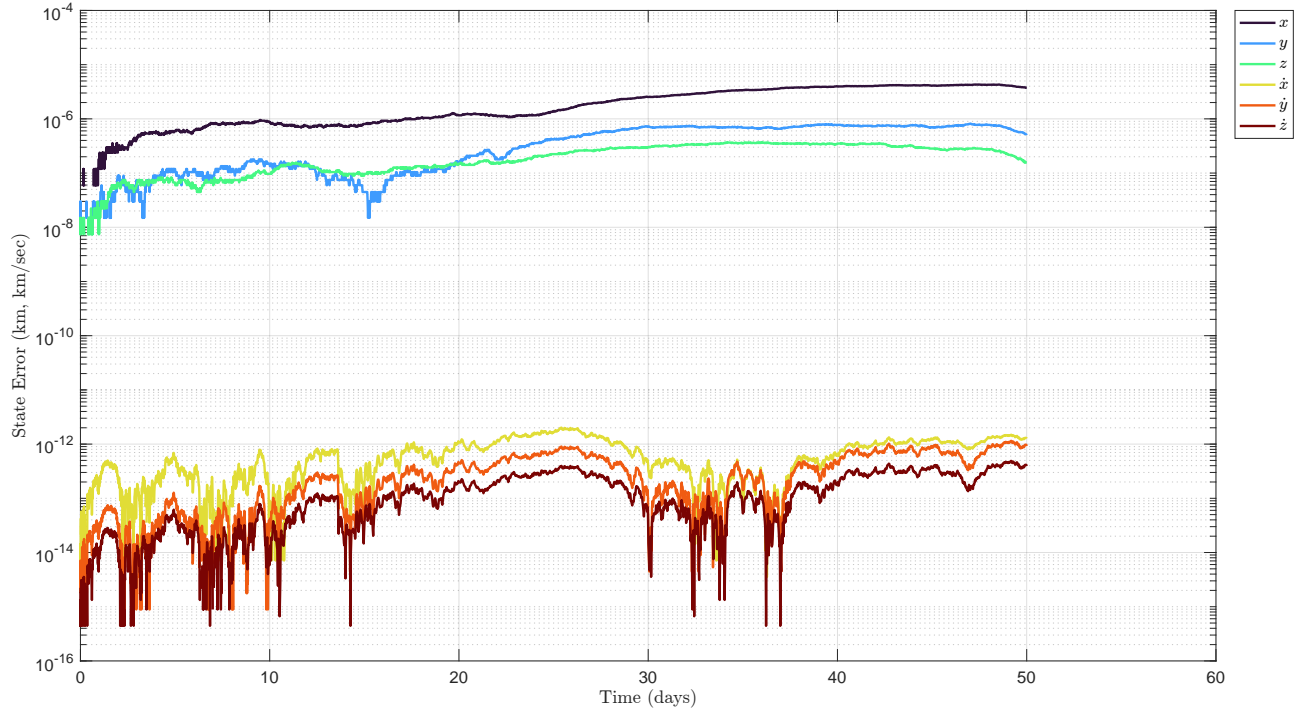
2.1 Dynamics Model

The spacecraft dynamics include Earth point mass gravity ($\mu_E = 398600.432896939 \text{ km}^3/\text{s}^2$), Sun point mass gravity ($\mu_S = 132712440017.987 \text{ km}^3/\text{s}^2$), and solar radiation pressure (SRP) modeled via a cannonball approximation. The SRP acceleration is modeled assuming an area-to-mass ratio (AMR) of $10^{-8} \text{ km}^2/\text{kg}$ and a reflectivity coefficient C_R equal to either 1.0 or 1.2, depending on the scenario. The initial epoch is set at JD = 2456296.25 (*i.e.*, 2013-Jan-03 18:00:00 UTC), during the spacecraft's inbound trajectory toward Earth, which is modeled as a perfect sphere with a radius of 6378.1363 km.

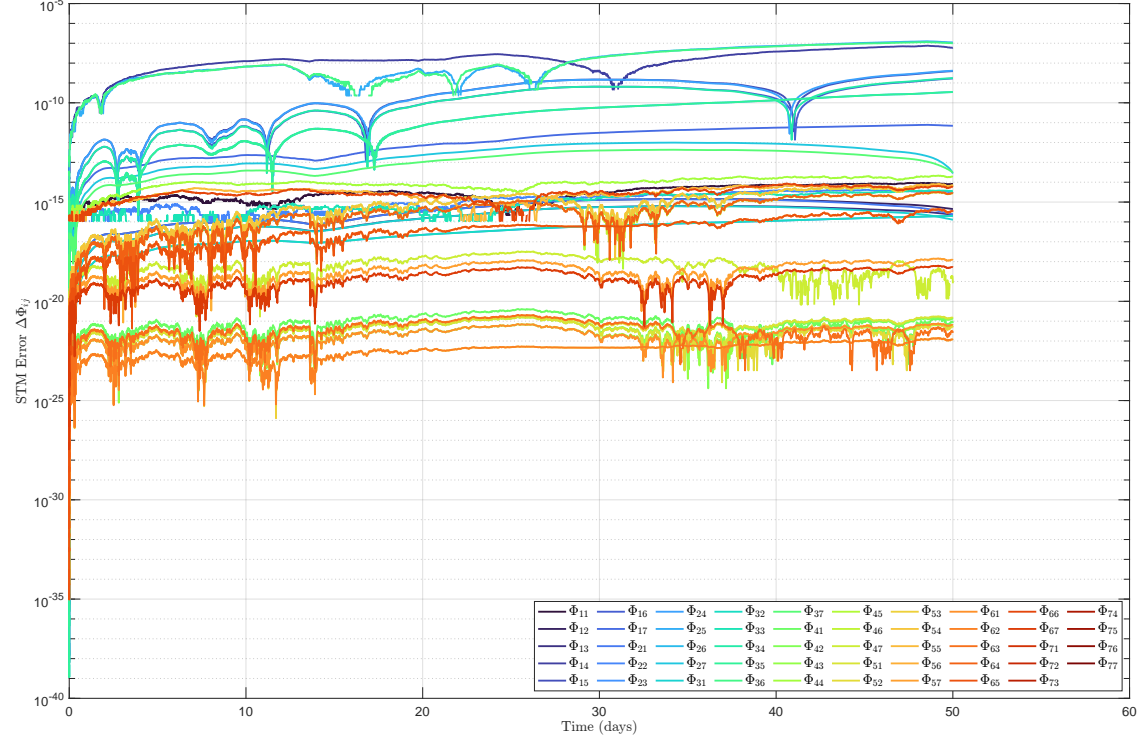
To validate the implementation of the dynamics model, the propagated trajectory and state transition matrix (STM) are compared against the instructor-provided truth data. The reference trajectory is integrated using a high-precision numerical setup: the `ode113` variable-step integrator is employed over the observation timespan, with tight relative and absolute tolerances of $\text{RelTol} = 2.22045 \times 10^{-14}$ and $\text{AbsTol} = 2.22045 \times 10^{-16}$, respectively. Excellent agreement is observed over the first 50 days of propagation, as shown in Figure 1, which illustrates the state and STM component errors.

2.2 Measurement Model

Radiometric tracking consists of range and range-rate observations from three Deep Space Network (DSN) ground stations: DSS 34 (Canberra), DSS 65 (Madrid), and DSS 13 (Goldstone). Measurement noise is modeled as 5 m on range and 0.5 mm/s on range-rate. The stations rotate with the Earth at a fixed rate of $\omega_E = 7.29211585275553 \times 10^{-5} \text{ rad/s}$ about the inertial z -axis, with an initial Greenwich angle of 0° .



(a) State error norm vs. time.



(b) STM components error vs. time.

Figure 1: Comparison between propagated dynamics and instructor-provided truth over the first 50 days.

3 Problem 2: Estimation with Known Models

3.1 Filter Setup

A batch least-squares estimator is employed to process the radiometric tracking data and estimate the spacecraft state. This approach is particularly appropriate for this portion of the project, as the dynamical and measurement models are assumed to be accurate and no process noise modeling is required. The batch formulation enables direct computation of the optimal state estimate by conditioning on the entire set of available observations, without the need for a sequential filter and smoothing architecture.

To improve numerical stability during the estimation, a square-root information filter (SRIF) formulation is adopted. Instead of explicitly forming and solving the normal equations of the form $\mathbf{A}\delta\mathbf{x} = \mathbf{n}$, the system is recast as

$$\mathbf{R}\delta\mathbf{x} = \mathbf{b},$$

where \mathbf{R} is the upper-triangular Cholesky factor of the information matrix and \mathbf{b} is the transformed right-hand side vector. The condition number of \mathbf{R} , $\mathcal{C}(\mathbf{R})$, satisfies

$$\mathcal{C}(\mathbf{R}) = \sqrt{\mathcal{C}(\mathbf{A})},$$

where $\mathcal{C}(\cdot)$ denotes the condition number. Consequently, the SRIF approach mitigates the amplification of round-off errors that would otherwise arise when solving the normal equations directly, leading to improved numerical robustness, especially for weakly observed parameters.

The a priori state vector at the initial epoch includes the spacecraft position \mathbf{r} , velocity \mathbf{v} , and reflectivity coefficient C_R , and is defined as:

$$\mathbf{x}_0 = \begin{bmatrix} -274096790.0 \text{ km} \\ -92859240.0 \text{ km} \\ -40199490.0 \text{ km} \\ 32.67 \text{ km/s} \\ -8.94 \text{ km/s} \\ -3.88 \text{ km/s} \\ 1.2 [-] \end{bmatrix}.$$

The a priori covariance matrix \mathbf{P}_0 is assumed diagonal, with standard deviations of 100 km for each position component, 0.1 km/s for each velocity component, and 0.1 for C_R :

$$\mathbf{P}_0 = \text{diag}([(100 \text{ km})^2, (100 \text{ km})^2, (100 \text{ km})^2, (0.1 \text{ km/s})^2, (0.1 \text{ km/s})^2, (0.1 \text{ km/s})^2, (0.1)^2]).$$

3.2 Goodness-of-Fit Assessment via Reduced Chi-Square Statistic

To quantitatively assess the consistency of the orbit determination solution, the reduced chi-square statistic, χ_{ν}^2 , is computed. The reduced chi-squared statistic is fundamentally a normalized Mahalanobis distance and serves as a standard statistical test for assessing the goodness-of-fit (GOF) between the estimated solution and the observed data. It is defined as

$$\chi_{\nu}^2 = \frac{1}{\nu} \mathbf{r}^\top \mathbf{W} \mathbf{r},$$

where \mathbf{r} is the vector of post-fit residuals, \mathbf{W} is the inverse of the measurement noise covariance matrix, and $\nu = m - n$ is the number of degrees of freedom, with m the number of measurements and n the number of estimated parameters. A χ_{ν}^2 value near unity indicates that the residuals are

statistically consistent with the assumed measurement error model. Values significantly greater than one suggest either underestimation of the measurement noise, model mismodeling, or unmodeled dynamic effects. Conversely, values significantly less than one may indicate overestimated measurement uncertainties or potential overfitting of the data. Although for the purposes of this project other consistency metrics and detailed analysis of post-fit residuals will provide deeper insight into the estimation performance, the reduced chi-square is included here for completeness as additional diagnostic tool for solution validity.

3.3 Results

The spacecraft trajectory corresponding to the Problem 2 scenario is shown in Figure 2. During the observed arc, the spacecraft remains inbound toward Earth but stays outside the three-sphere-of-influence ($3 \times \text{SOI}$) boundary. The dataset spans approximately 196 days, culminating at the data cutoff event (DCO).

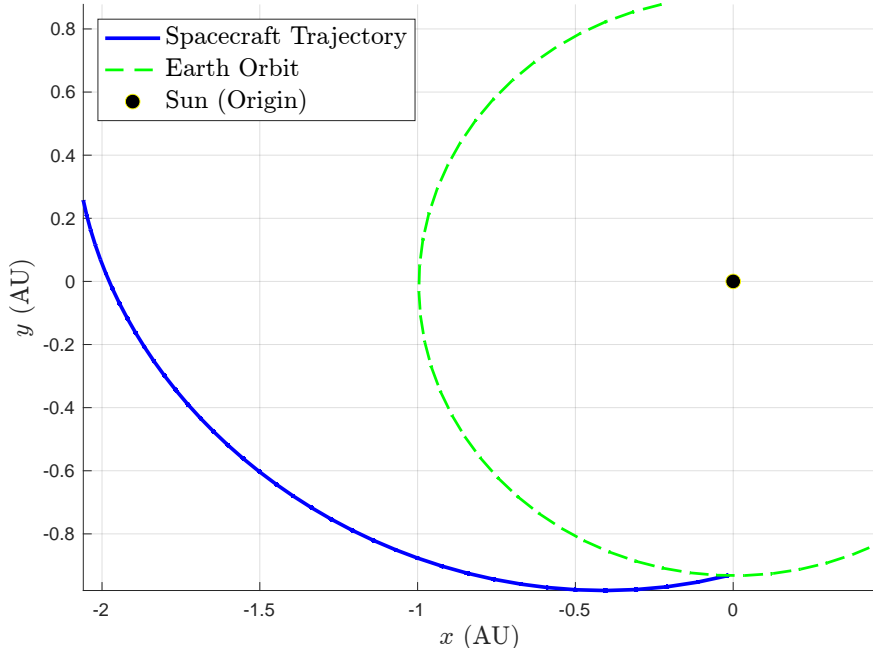


Figure 2: Spacecraft inbound trajectory toward Earth for Problem 2.

The solution quality is assessed by analyzing the time evolution of the $3 - \sigma$ envelopes, shown in Figure 3¹. Only two batch SRIF iterations are performed, as convergence is effectively achieved after the first; the second is included for completeness. Despite the relatively long observational arc, the batch fit remained numerically stable, with a final reciprocal condition number $\kappa_r = 5.77 \times 10^{-25}$ —near the limits of acceptable conditioning but sufficient to avoid arc segmentation.

The solution obtained here serves as a benchmark case, as no process noise is introduced. While slightly longer datasets are considered in subsequent scenarios, this case represents an idealized estimation environment and establishes a lower bound on the achievable state covariance. At the end of the arc, the $3 - \sigma$ position uncertainty is below 1 meter and the $3 - \sigma$ velocity uncertainty is

¹It is noted that the covariance envelopes are more general for sequential filtering frameworks where time-varying parameters are estimated. In a batch filter, for instance, C_R is constant; however, these plots are included for completeness and comparability across estimation strategies.

below 0.1 millimeter per second, highlighting the high accuracy achievable under perfect modeling assumptions.

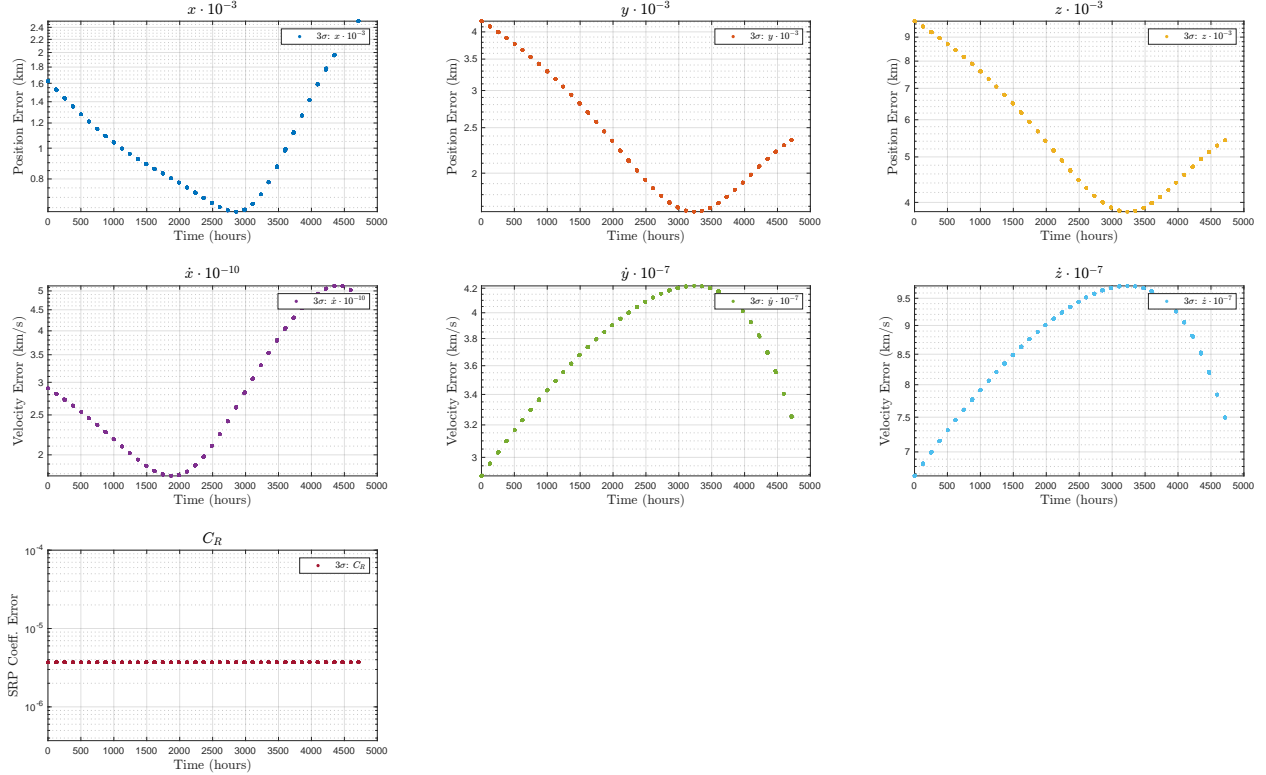


Figure 3: 3- σ covariance envelopes for estimated states over the observation arc.

Pre-fit and post-fit residuals are illustrated in Figures 4 and 5. The pre-fit residuals initially exhibit significant biases, with range residuals reaching magnitudes on the order of 10^4 kilometers toward the end of the arc. After two filter iterations, the post-fit residuals are effectively white, zero-mean, and fully consistent with the assumed measurement noise spectral density. The reduced chi-square value for the final solution is $\chi^2_\nu = 0.998530$, confirming excellent statistical consistency between the post-fit residuals and the declared measurement uncertainties. Although a rigorous orbit determination process would typically require evaluating the non-linear residuals to verify full convergence, such validation is not necessary in this idealized test case, which is intended primarily as preparation for the following section. In practical applications, further verification using alternate filter configurations, varied datasets, overlapping arcs, and consistency checks across independent solutions would be advisable. For the purposes of this benchmark scenario, however, the current results are considered satisfactory.

Finally, B-plane mapping results are shown in Figure 6. Each batch SRIF solution (after processing 50, 100, 150, and 200 days of data, respectively) is propagated to the B-plane intersection. The 200-days DCO occurs at approximately 197 days; the spacecraft crosses the $3 \times$ SOI boundary at roughly 275 days, and the B-plane intersection is identified via event detection at approximately 278 days. As expected, increasing the number of processed measurements leads to a reduction in the size of the B-plane uncertainty ellipse. Each updated estimate remains well within the $3 - \sigma$ uncertainty region of the previous, shorter-arc solution, confirming the internal consistency of the estimation process. Notably, a substantial improvement is observed between the 50-day and 100-day solutions, whereas marginal improvement occurs between the 150-day and 200-day solutions. The

final B-plane uncertainty ellipse has a semi-major axis on the order of a few kilometers, indicating an extremely high-quality targeting solution.

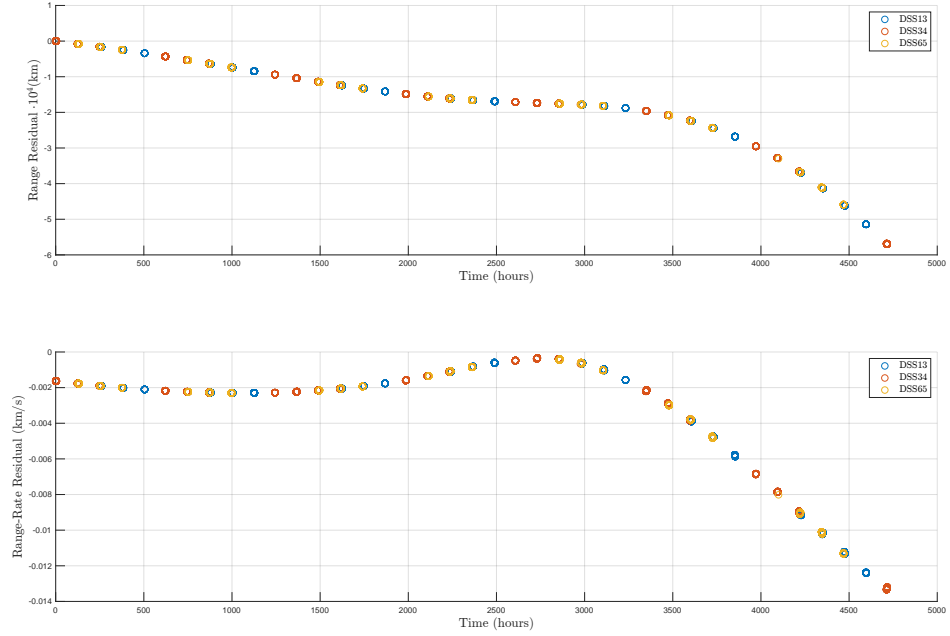


Figure 4: Pre-fit residuals for range and range-rate measurements.

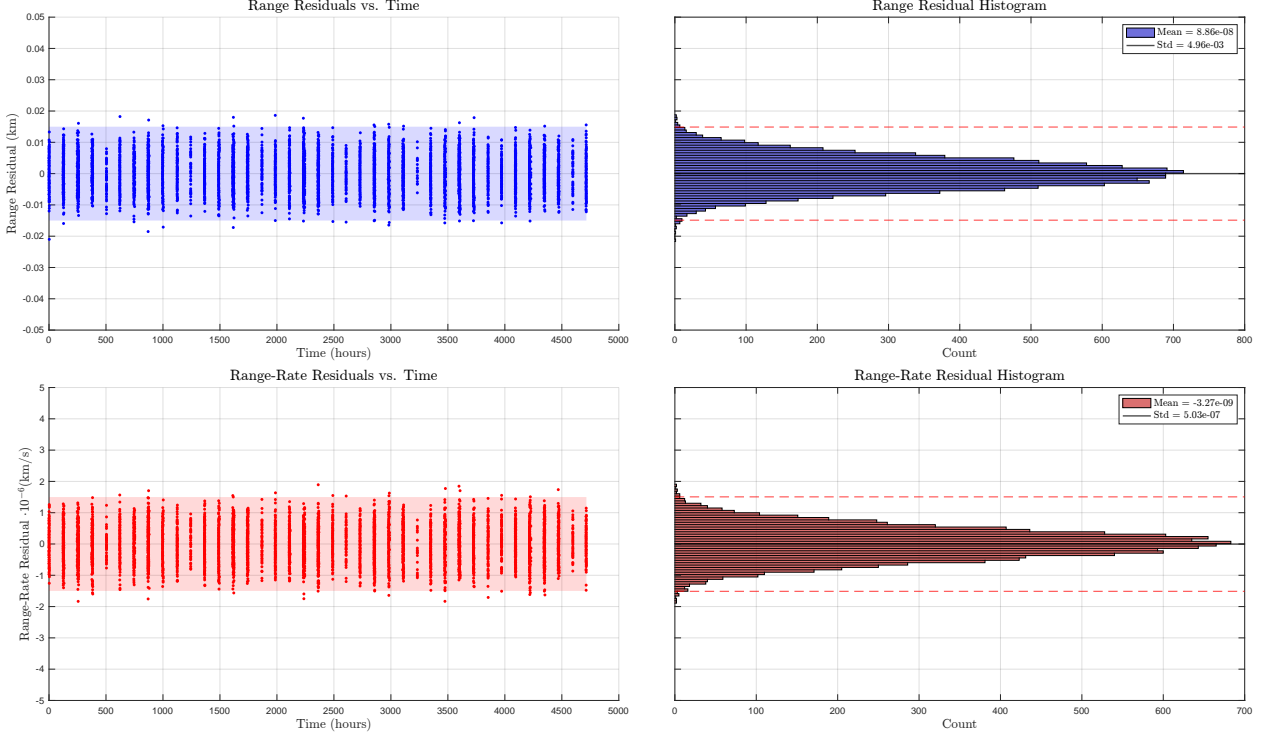


Figure 5: Post-fit residuals for range and range-rate measurements.

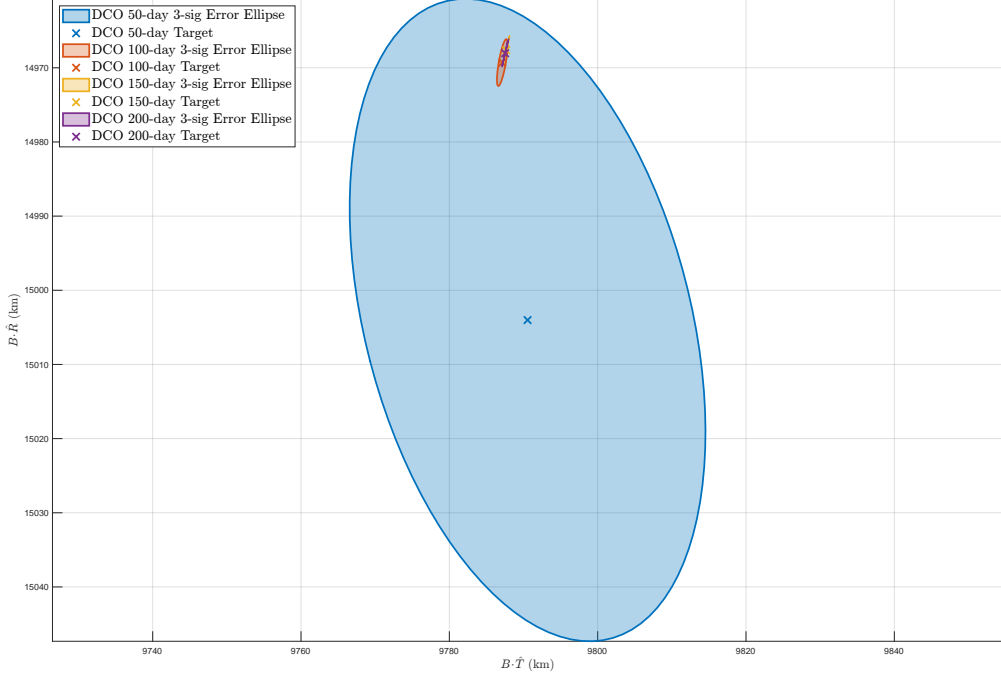


Figure 6: B-plane uncertainty mapping after 50, 100, 150, and 200 days of tracking.

4 Problem 3: Estimation with Unknown Errors

4.1 Filter Setup and Strategy

The minimum set of estimated parameters consists of the spacecraft position \mathbf{r} , velocity \mathbf{v} , and the reflectivity coefficient C_R . The a priori state vector is initialized as

$$\mathbf{x}_0 = \begin{bmatrix} -274096770.76544 \text{ km} \\ -92859266.4499061 \text{ km} \\ -40199493.6677441 \text{ km} \\ 32.6704564599943 \text{ km/s} \\ -8.93838913761049 \text{ km/s} \\ -3.87881914050316 \text{ km/s} \\ 1.0 [-] \end{bmatrix}.$$

The a priori covariance matrix is identical to that adopted in Problem 2, with standard deviations of 100 km for each position component, 0.1 km/s for each velocity component, and 0.1 for C_R .

Unlike in Problem 2, process noise will be incorporated to model potential dynamical mismodelling. Consequently, sequential filtering approaches are primarily employed. In particular, three estimation strategies are considered: a batch SRIF as a first naive attempt, a Linearized Kalman Filter (LKF) combined with a Rauch-Tung-Striebel (RTS) smoother, and a sequential SRIF. While the SRIF offers superior numerical stability, time constraints associated with implementing a corresponding SRIF-based smoother limited its use for primary results, and it is instead utilized primarily for consistency checks.

The LKF+RTS configuration constitutes the principal approach in this analysis. Sequential filtering enables the incorporation of either spectrally white process noise (Sequential Noise Compensation, SNC) or temporally correlated noise (Dynamic Model Compensation, DMC). The RTS

smoother, in turn, yields a batch-like solution, wherein each estimated state benefits from the conditioning provided by all available measurements across the arc, while preserving the flexibility to handle process noise modeling.

4.2 Preliminary Residual and Trajectory Inspection

To diagnose the sources of modeling errors present in Problem 3, an initial analysis of the post-fit residuals is conducted using two different estimators: a batch SRIF and a LKF without a smoother. The sequential filter is executed without the inclusion of process noise at this stage. The objective of this preliminary investigation is to characterize the structure of the residuals, assess the level of dynamical mismodeling, and inform the design of subsequent filtering strategies. The spacecraft’s nominal trajectory, propagated from the a priori state without correction, is shown in Figure 7. The trajectory exhibits the expected EGA configuration, with a Data Cut-Off (DCO) occurring approximately two weeks later than in Problem 2.

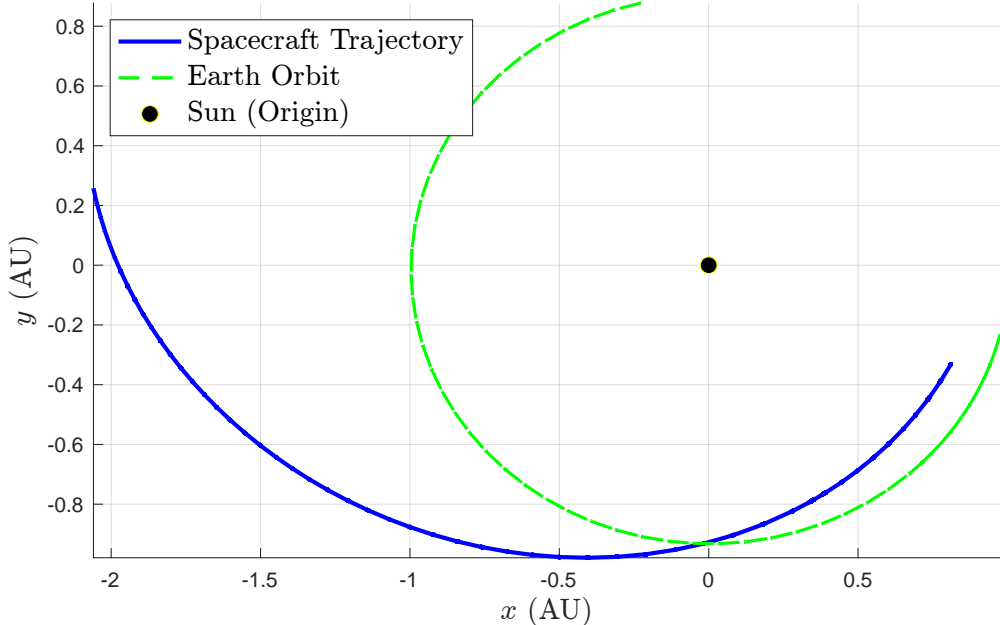


Figure 7: Initial spacecraft trajectory for Problem 3 based on a priori state.

The pre-fit residuals are qualitatively similar to those observed in Problem 2, exhibiting large biases due to initial condition errors at the epoch t_0 , and are therefore omitted. Figures 8 and 9 present the post-fit residuals obtained from the batch SRIF solution and the LKF, respectively. In both cases, the post-fit residuals reveal systematic biases and low-frequency trends, indicating significant dynamical mismodeling, unaccounted forces, or possible miscalibration within the measurement model.

The batch SRIF post-fit residuals exhibit large-scale errors (*i.e.*, an average of 50 km in range and 0.5 km/s in range rate) that persist throughout the arc, confirming the presence of modeling inaccuracies. Since the batch filter estimates the best-fit state at the reference epoch and then propagates the solution forward, the residuals reflect an average model mismatch over the arc. A low-frequency periodic signature is evident in the range residuals, characterized by a semi-sinusoidal pattern with approximately eight peaks spanning the eight-month observational arc. The range-rate residuals show that the spacecraft appears to move radially faster toward the ground stations

before crossing Earth’s orbit and slower afterward.

The LKF post-fit residuals, by contrast, reveal more localized mismodeling effects. Toward the end of the arc, a significant anomaly appears, likely corresponding to an unmodeled maneuver. Additional small discontinuities earlier in the trajectory suggest minor dynamical events (at least one other maneuver), although these will likely be masked once process noise is introduced. Examination of the estimated C_R parameter (not shown) further indicates that the filter attempts to absorb some unmodeled effects by significantly adjusting C_R at certain times, reaching unphysical values (*e.g.*, dropping below -4 or exceeding 2). A closer inspection of the residuals reveals that measurements at the start of each observation mini-arc—following a data gap—often fall outside the $3 - \sigma$ bounds, gradually re-entering as the filter assimilates new measurements.

It is important to note that these post-fit residuals are based on a linearized dynamical model and may differ from those obtained through full nonlinear propagation. Nonetheless, batch filters or smoothing applied after the LKF tend to distribute modeling errors over the estimation arc, often masking them as initial state biases. Consequently, interpreting residual signatures remains nontrivial and typically requires either a high-fidelity a priori estimate or pre-event signature simulations, as demonstrated in the Juno mission prior to its EGA.

Assuming that at least one significant maneuver is present (as suggested by the residuals), the key question remains how to address the general modeling errors. Several potential sources are investigated. Dynamical parameters such as the Earth’s gravitational parameter μ_E or the Sun’s μ_S are considered, but these would likely manifest as a secular bias rather than a periodic monthly oscillation. The monthly signature could point toward third-body effects, such as lunar gravity, but lunar perturbations are excluded by project instructions. Minor inaccuracies in the solar ephemeris, modeled as the negative deviation from the Earth’s two-body motion around the Sun, are also examined but did not resolve the issue. Modeling errors in the SRP force would typically be absorbed through adjustments to the estimated C_R parameter; however, this mechanism appears insufficient to account for the residuals observed. Alternative modeling approaches are investigated, including the introduction of well-established non-gravitational force models from astrometry (*e.g.*, $\mathbf{a}_{ng}(t) = g(\mathbf{r})(A_1 \hat{\mathbf{t}} + A_2 \hat{\mathbf{r}} + A_3 \hat{\mathbf{n}})$, with $g(\mathbf{r}) = 1/r^2$), as well as the fitting of periodic (Fourier-based) force components aligned with the Sun direction. Nevertheless, these modifications did not yield a significant improvement in the residual structure. Measurement model errors, such as biases in station locations or errors in Earth Orientation Parameters (EOP) or Julian Date (JD_0), are also considered. However, these would typically produce daily or diurnal residual patterns rather than monthly ones.

Thus, while ideally the underlying dynamical model discrepancies would be identified and corrected, project time constraints require a more pragmatic approach. In the following sections, process noise modeling will be introduced to absorb residual modeling errors and enable statistically consistent filtering despite incomplete dynamical representation. While this approach compromises the ability to rigorously assess convergence via nonlinear pre-fit residuals—and yields a less accurate B-plane projection due to the reliance on forward propagation—it is considered an acceptable trade-off in light of the study’s primary objectives.

4.2.1 Impulsive Burn Modeling

To improve the solution accuracy, the maneuver occurring approximately two-thirds into the dataset is explicitly modeled. The adopted strategy introduces the impulsive maneuver directly into the

dynamical model and filter formulation. The state vector is defined as

$$\mathbf{x} = \begin{bmatrix} \mathbf{r} \\ \mathbf{v} \\ C_R \\ \Delta\mathbf{v} \\ t_b \end{bmatrix},$$

where $\Delta\mathbf{v}$ is the impulsive velocity change, and t_b is the corresponding maneuver epoch. Although this state vector is propagated continuously throughout the estimation arc, the $\Delta\mathbf{v}$ and t_b components only affect the dynamics after the maneuver time. This behavior is enforced by modifying the State Transition Matrix (STM) at t_b , ensuring that correlations are correctly propagated through the deviation dynamics. The modeling approach consists of the following key elements:

1. The integration is stopped at the maneuver epoch t_b , where an instantaneous velocity change $\Delta\mathbf{v}$ is applied to the velocity components.
2. Both the maneuver vector and its timing are estimated as part of the filter state by modifying the STM to include the corresponding partial derivatives:
 - The partial derivative of the propagated position and velocity with respect to the maneuver epoch t_b is defined as

$$\Phi_{\mathbf{rv}, t_b}(t_b, t_0) = \Phi_{\mathbf{rv}}(t_b, t_0) \begin{bmatrix} -\Delta\mathbf{v} \\ \mathbf{0} \end{bmatrix},$$

where $\Phi_{\mathbf{rv}}$ denotes the portion of the STM mapping the initial position and velocity at t_0 to their values at the maneuver epoch t_b .

- The partial derivative of the propagated position and velocity with respect to the impulsive burn vector $\Delta\mathbf{v}$ is

$$\Phi_{\mathbf{rv}, \Delta\mathbf{v}}(t_b, t_0) = \Phi_{\mathbf{rv}}(t_b, t_0) \begin{bmatrix} \mathbf{0} \\ \mathbf{I} \end{bmatrix}.$$

3. Propagation is resumed using the updated initial conditions and the modified STM.
4. While partial derivatives of the measurements with respect to the maneuver parameters may be non-zero in principle (e.g., $\Delta\mathbf{v}$ affecting Doppler observable), they are typically neglected since the maneuver does not occur exactly at a measurement time. In practice, four zeros are appended to the measurement sensitivity vector. Moreover, during real spacecraft operations, attitude constraints during thrusting arcs often prevent tracking.

4.2.2 Process Noise Modeling

Regarding broader dynamical modeling errors, one hypothesis is that inaccuracies may stem from treating the C_R parameter as constant, despite the possibility that it varies dynamically over time. For instance, a spin-stabilized spacecraft like Juno would naturally exhibit variations in effective C_R due to changes in its projected area. However, the observed monthly oscillation pattern is not characteristic of spin-induced fluctuations, which typically occur on much shorter timescales. This discrepancy suggests that the observed behavior may instead be attributed to another unmodeled external force. Further investigation into the origin of these errors is conducted using both State

Noise Compensation (SNC) and Dynamical Model Compensation (DMC) techniques. In the DMC framework, the state vector is modified to include empirical acceleration components w_x, w_y, w_z , each modeled as a first-order Gauss–Markov process governed by the Langevin equation:

$$\dot{\mathbf{w}} = -\mathbf{B}\mathbf{w},$$

where $\mathbf{B} = \text{diag}(1/\tau_x, 1/\tau_y, 1/\tau_z)$ is the diagonal matrix of decay rates, with τ_i representing the correlation time associated with each empirical acceleration component. This formulation introduces process noise on the time derivative of the empirical acceleration, effectively modeling uncertainty at the jerk level. In contrast, the SNC approach applies process noise directly to the acceleration vector itself, without modeling its temporal evolution explicitly.

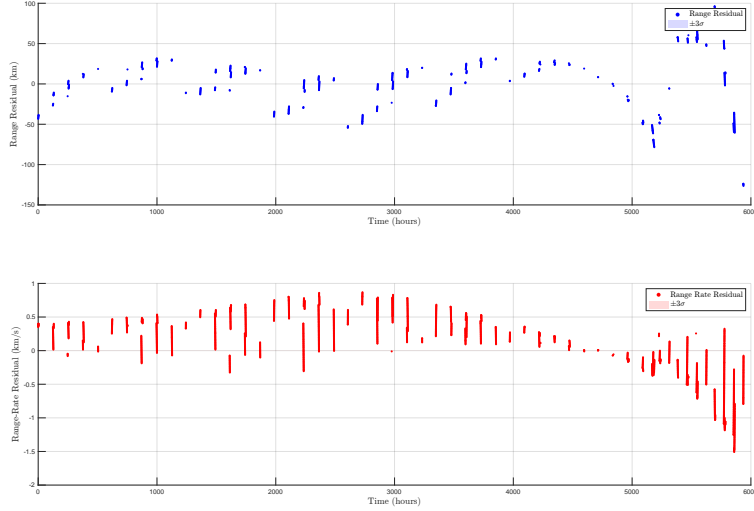


Figure 8: Post-fit residuals from batch SRIF.

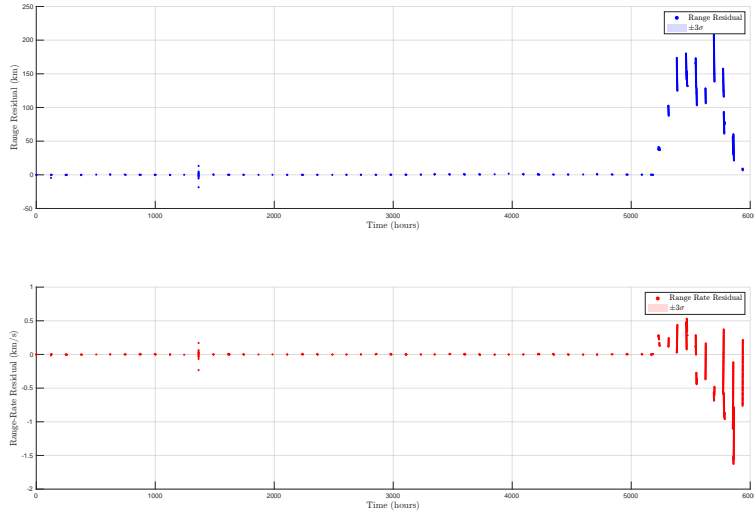


Figure 9: Post-fit residuals from LKF.

4.2.3 Note on Propagation to the B-plane

Rather than relying on a fixed forward propagation interval (e.g., $[0, \text{LTOF}]$), the B-plane crossing is identified via an event function that monitors when the position vector becomes perpendicular to the incoming asymptote, *i.e.*, when $\mathbf{r} \cdot \hat{\mathbf{S}} = 0$. This ensures more accurate detection of the actual B-plane intersection.

4.3 Results

The results are organized into five OD cases², each employing a distinct filtering and modeling strategy to address the challenges posed by Problem 3:

- **OD03**: Applies DMC to the first 75% of the dataset, deliberately excluding the maneuver event in order to isolate and characterize unmodeled dynamical effects. Estimation is performed using a two-iteration LKF with RTS smoothing. The state vector includes $[\mathbf{r}, \mathbf{v}, C_R, \mathbf{w}]^\top \in \mathbb{R}^{10}$.
- **OD02**: Incorporates SNC over the full dataset while explicitly modeling the main maneuver. Estimation is again performed using a two-iteration LKF+RTS. The state vector is defined as $[\mathbf{r}, \mathbf{v}, C_R, \Delta\mathbf{v}, t_b]^\top \in \mathbb{R}^{11}$.
- **OD01**: Combines DMC and explicit maneuver modeling across the entire dataset, using two LKF+RTS iterations for estimation. The state vector includes $[\mathbf{r}, \mathbf{v}, C_R, \Delta\mathbf{v}, t_b, \mathbf{w}]^\top \in \mathbb{R}^{14}$.
- **OD04**: Mirrors the *OD02* configuration but replaces the LKF+RTS with a two-iteration Square Root Information Filter (SRIF) to validate the consistency of the *OD02* results. The state vector remains $[\mathbf{r}, \mathbf{v}, C_R, \Delta\mathbf{v}, t_b]^\top \in \mathbb{R}^{11}$.
- **OD05**: Repeats the *OD03* setup but extends the DMC application to the full dataset, thereby omitting explicit maneuver modeling. This allows an evaluation of the maneuver's impact. The state vector is again $[\mathbf{r}, \mathbf{v}, C_R, \mathbf{w}]^\top \in \mathbb{R}^{10}$.

One of these solutions is selected as the nominal OD result based on a comprehensive evaluation of residual statistics, filter consistency, and additional performance metrics. Final results are reported accordingly. While a batch filter is generally preferred due to its favorable conditioning and global consistency, its lack of native support for stochastic process modeling limits its applicability here. Although a SRIF combined with its corresponding smoother would offer enhanced numerical robustness, implementing a SRIF smoother capable of handling DMC (*i.e.*, correlated noise models) is not feasible within the current time constraints. Ideally, the most rigorous formulation would involve a pseudo-epoch SRIF with batched stochastic modeling (*i.e.*, a batched DMC approach), which remains a direction for future work.

4.3.1 **OD03: LKF+RTS Filtering with DMC on First 75% of the Arc**

DMC is applied to the first 75% of the available tracking dataset to gain better insight into unmodeled dynamical effects while intentionally avoiding the explicit modeling of the maneuver, which could otherwise interfere with or be absorbed by the DMC process. Estimation is performed using a two-iteration LKF followed by RTS smoothing. The estimated state vector is defined as $[\mathbf{r}, \mathbf{v}, C_R, \mathbf{w}]^\top$.

²The numerical identifiers of the OD solutions do not correspond to their order of execution, as the analyses are performed at different stages during development.

DMC tuning identified an optimal decorrelation time constant of $\tau_i = 60$ days, consistent with the approximate two-month periodicity discussed in a previous section. The continuous-time process noise standard deviation is set to $q_w = 10^{-11}$ km/s³, yielding a process noise matrix $\mathbf{Q}(t) = q_w \mathbf{I}_{3x3}$, which is a typical magnitude for stochastic spacecraft accelerations. The empirical acceleration components are initialized at zero with an a priori standard deviation of 10^{-9} km/s².

The time evolution of the $3 - \sigma$ bounds for all estimated state components is presented in Figure 10. Compared to the previous idealized case without process noise, the covariance bounds here are noticeably larger, reflecting the uncertainty introduced by allowing stochastic model compensation. The position uncertainty reaches a minimum on the order of several hundred kilometers, emphasizing the critical importance of precise dynamical modeling in operational orbit determination. In addition, velocity uncertainties, which were previously below the millimeter-per-second level, now generally remain below 1 m/s.

Post-fit residuals for range and range-rate measurements are shown in Figure 11. The residuals are bounded within the $3 - \sigma$ noise envelope and exhibit white noise behavior, indicating a good fit. Histograms of the residuals confirm near-zero means and the absence of significant outliers. The reduced chi-squared value is $\chi^2_\nu = 0.8697$, suggesting a slight overfitting relative to the assumed noise model. It is worth noting that although a third iteration could be performed to analyze non-linear pre-fit residuals—a standard practice in OD to assess solution quality—the presence of significant unmodeled dynamics, absorbed through the DMC process, would limit the usefulness of such a diagnostic. In this context, the absence of an accurate dynamical model would result in poor predictive performance, and the non-linear pre-fit residuals would remain biased regardless of filter convergence.

The evolution of the empirical accelerations (w_x, w_y, w_z) estimated by the filter is shown in Figure 12. These components act to absorb unmodeled perturbations. While their values are centered around zero, their magnitude remains comparable to the dynamics of the system: on the order of 10^{-9} km/s², which is smaller than solar gravity (10^{-5}) but comparable to SRP (10^{-10}) and Earth third-body effects (10^{-11}). This supports the presence of persistent unmodeled forces. Further evidence is provided in Figure 13, where the mean of a moving average over varying window lengths reveals a non-zero trend in the empirical acceleration magnitude.

A Fourier analysis of the empirical acceleration magnitude is presented in Figure 14. The spectrum reveals dominant low-frequency components, notably peaks corresponding to periods of approximately 17.95, 26.93, and 53.87 days. This again suggests the presence of slowly varying, periodic unmodeled forces consistent with the observed monthly to bimonthly behavior.

The time evolution of the empirical acceleration azimuth and elevation angles, relative to the ECI frame, is shown in Figure 15. While the magnitude exhibits clear oscillations, the directional behavior is less structured, with large swings, sometimes exceeding hundreds of degrees away from the equatorial plane. This behavior is typical for DMC estimations, where the empirical forces attempt to compensate for multiple overlapping dynamical errors.

Finally, Figure 16 presents the distribution of the cosine of the angles between the empirical acceleration vector and the Sun and Earth directions. A moderate correlation with the Sun direction is observed, supporting the hypothesis that the unmodeled forces are at least partially aligned with the solar vector. While a full physical interpretation remains nontrivial, this directional alignment reinforces the exploratory findings that incorporating empirical force components aligned with the Sun direction can enhance estimation performance. In particular, a parametric model consisting of Fourier-modulated Sun radial accelerations of the form $\mathbf{a}_F(t) = g(\mathbf{r}) \left[\sum_{k=1}^K \alpha_k \cos(k\omega t) + \beta_k \sin(k\omega t) \right] \hat{\mathbf{r}}_{\text{Sun}}$, with $\omega = 2\pi/30$ days, were found to be especially sensitive in trial runs.

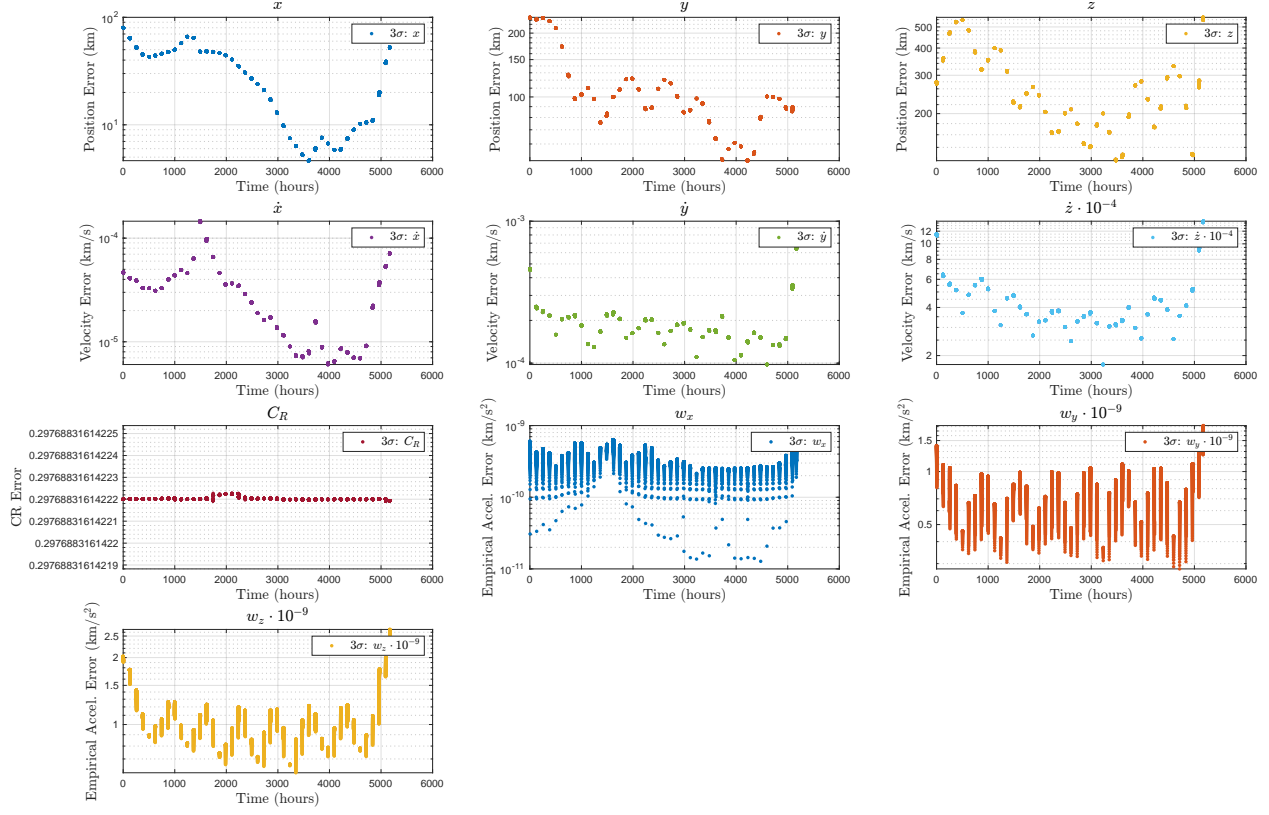


Figure 10: 3σ covariance envelopes for estimated states (OD03).

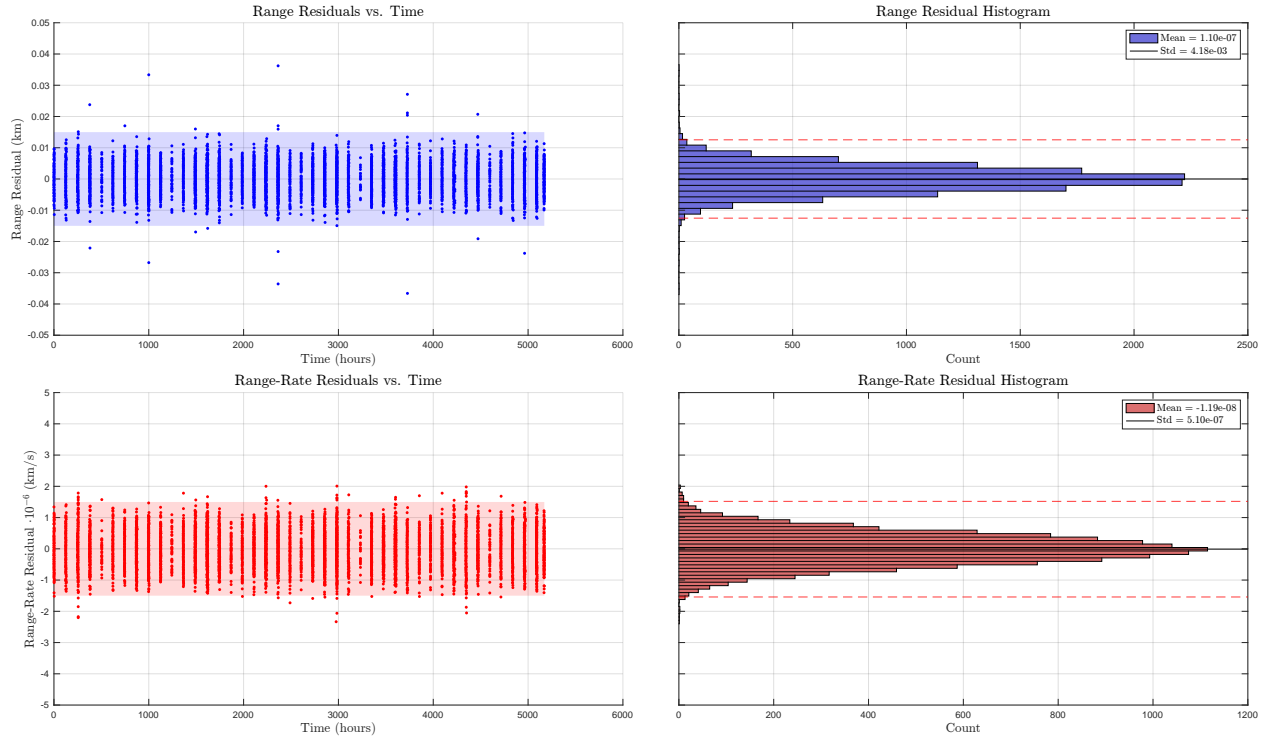


Figure 11: Post-fit residuals for range and range-rate measurements (OD03).

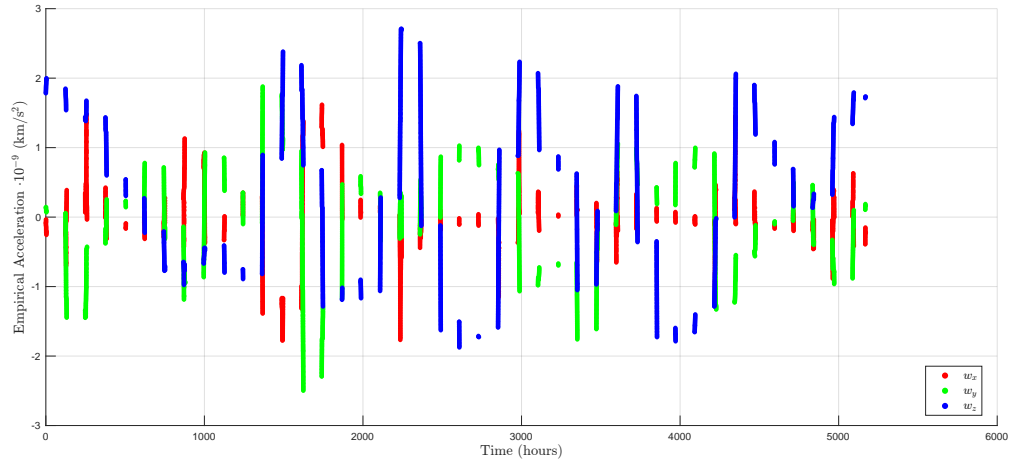


Figure 12: Estimated empirical accelerations during *OD01*.

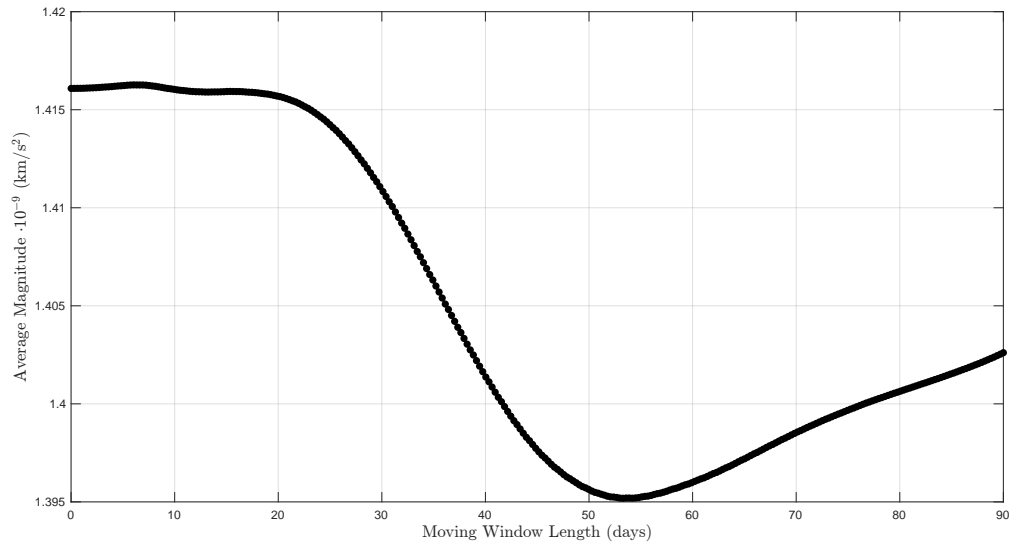


Figure 13: Mean of moving average of empirical acceleration magnitude as a function of window size (*OD03*).

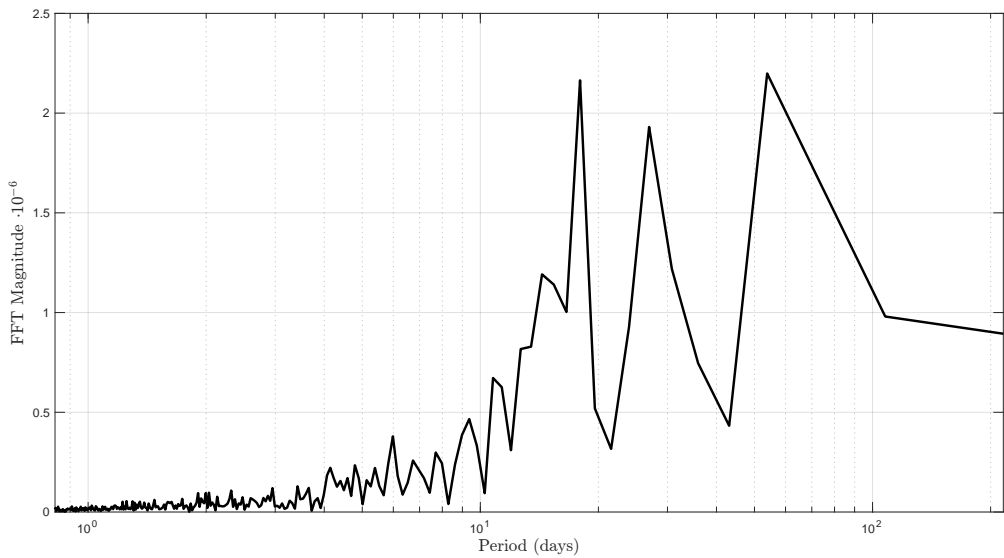


Figure 14: Fourier spectrum of empirical acceleration magnitude (*OD03*).

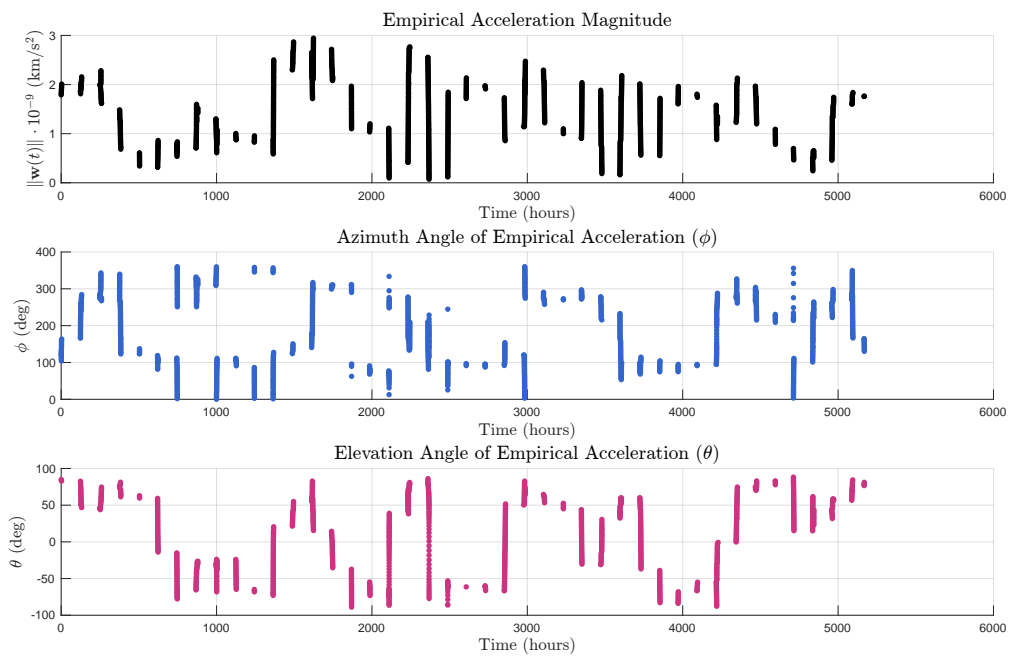


Figure 15: Azimuth and elevation angles of empirical accelerations (*OD03*).

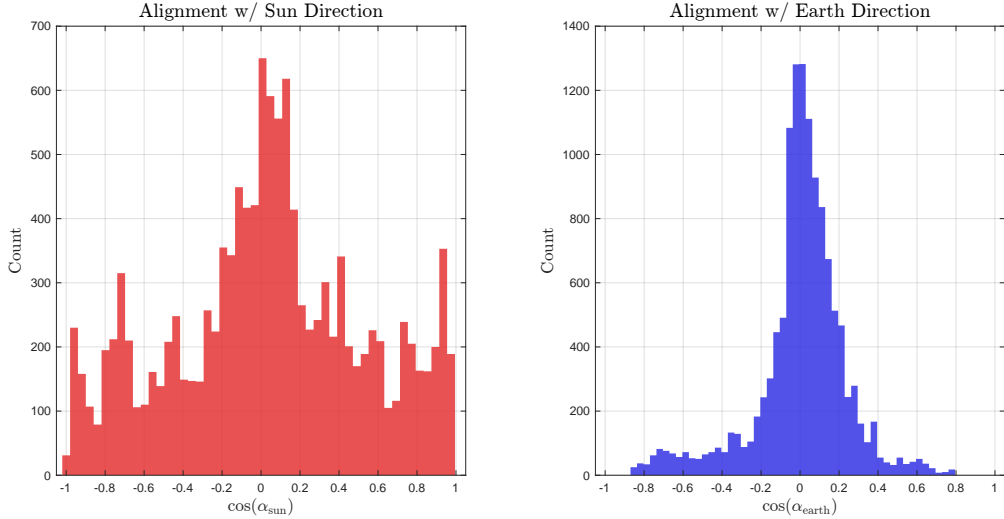


Figure 16: Cosine of alignment between empirical accelerations and Sun and Earth directions (*OD03*).

4.3.2 *OD02*: LKF+RTS Filtering with SNC and Maneuver Modeling

In this case, the main maneuver is explicitly modeled within the filter, while SNC is employed to account for small residual unmodeled accelerations without explicitly estimating their profiles. Through SNC, the filter compensates by assigning greater trust to the measurements relative to the dynamical model, acknowledging the presence of potential model deficiencies. Estimation is again performed using a two-iteration LKF followed by RTS smoothing. The estimated state vector is defined as $[\mathbf{r}, \mathbf{v}, C_R, \Delta\mathbf{v}, t_b]^\top$.

While *OD01* produced a statistically consistent solution, explicit maneuver modeling is necessary because, if unmodeled, a maneuver would induce major deviations in the B-plane targeting, far exceeding the errors arising from missing continuous small accelerations. Proper $\Delta\mathbf{v}$ modeling is thus critical for achieving accurate trajectory reconstructions.

In this configuration, the continuous-time process noise spectral density for SNC is set to $q_u = 10^{-8} \text{ km}^2/\text{s}^4$. The impulsive maneuver vector $\Delta\mathbf{v}$ is initialized at zero, with the maneuver epoch placed at 5200 hours into the arc. The initial uncertainty on the components of $\Delta\mathbf{v}$ is set to 10^{-4} km/s , while the a priori uncertainty on the maneuver epoch t_b is initialized at 10^3 seconds. The estimated maneuver parameters are reported in Table 1.

The time evolution of the $3-\sigma$ covariance bounds for all estimated states is shown in Figure 17. Compared to *OD03*, the overall uncertainty levels remain similar, reflecting the application of a comparable level of process noise. Distinct spikes appear in the y and z components of position and velocity at the maneuver epoch, as expected from the impulsive $\Delta\mathbf{v}$ event. Following the maneuver, the uncertainties in Δv_i change markedly—either increasing or decreasing—as expected, indicating where the maneuver begins to influence the system dynamics. In contrast, the maneuver epoch t_b exhibits poor observability, with its uncertainty remaining high and unchanged. This suggests that the maneuver vector may have been oriented such that it had limited projection onto the line-of-sight direction.

The uncertainty on the SRP coefficient C_R decreases relative to *OD01* due to the absence of DMC; however, without empirical acceleration terms to absorb model deficiencies, the filter compensates by over-adjusting C_R , driving its estimate to an unphysical value of 2.224.

Post-fit residuals for range and range-rate measurements are shown in Figure 18. The range

residuals are largely bounded within the $3-\sigma$ noise envelope and exhibit white noise behavior, while the range-rate residuals display signs of overfitting and include a significant number of outliers. Although a color-coded analysis by ground station could provide further insight (*e.g.*, Doppler biases), this is left for future investigation. The absence of pronounced residual spikes at the maneuver time confirms that the impulsive Δv model is correctly implemented. Nonetheless, the persistent structure in the Doppler residuals points to remaining unmodeled forces.

The reduced chi-squared statistic for this solution is $\chi^2_\nu = 1.0543$, which might misleadingly suggest an excellent fit. In this case, the residual distribution fails to fully capture the qualitative discrepancies visible in the time series. These findings motivate the hybrid strategy adopted in *OD01*, where explicit maneuver modeling is complemented by DMC to better accommodate dynamical mismodeling.

Table 1: Estimated Maneuver Parameters and $1-\sigma$ Uncertainties (*OD02*)

Parameter	Estimated Value	$\pm 1\sigma$	Units
Δv_x	8.6219×10^{-5}	2.3331×10^{-7}	km/s
Δv_y	-2.5499×10^{-4}	1.7779×10^{-6}	km/s
Δv_z	2.3339×10^{-4}	3.9368×10^{-6}	km/s
t_b	5199.96	0.2778	hr

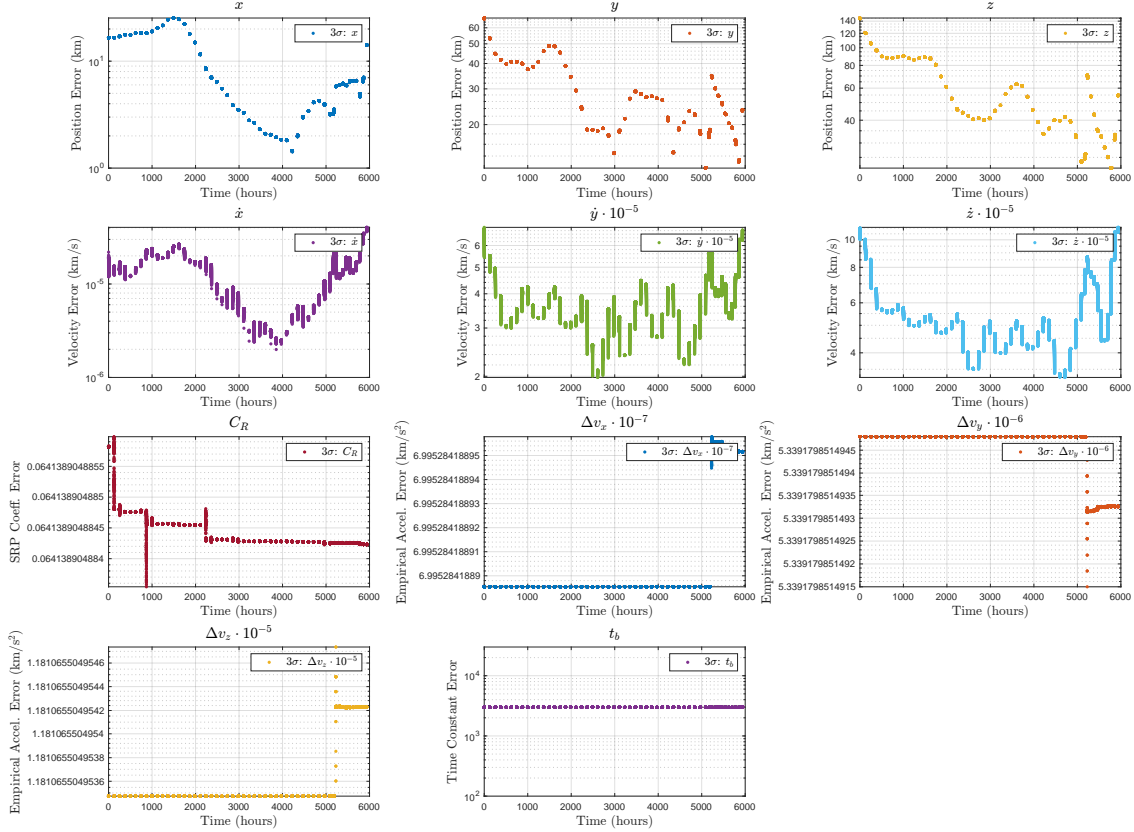


Figure 17: $3-\sigma$ covariance envelopes for estimated states (*OD02*).

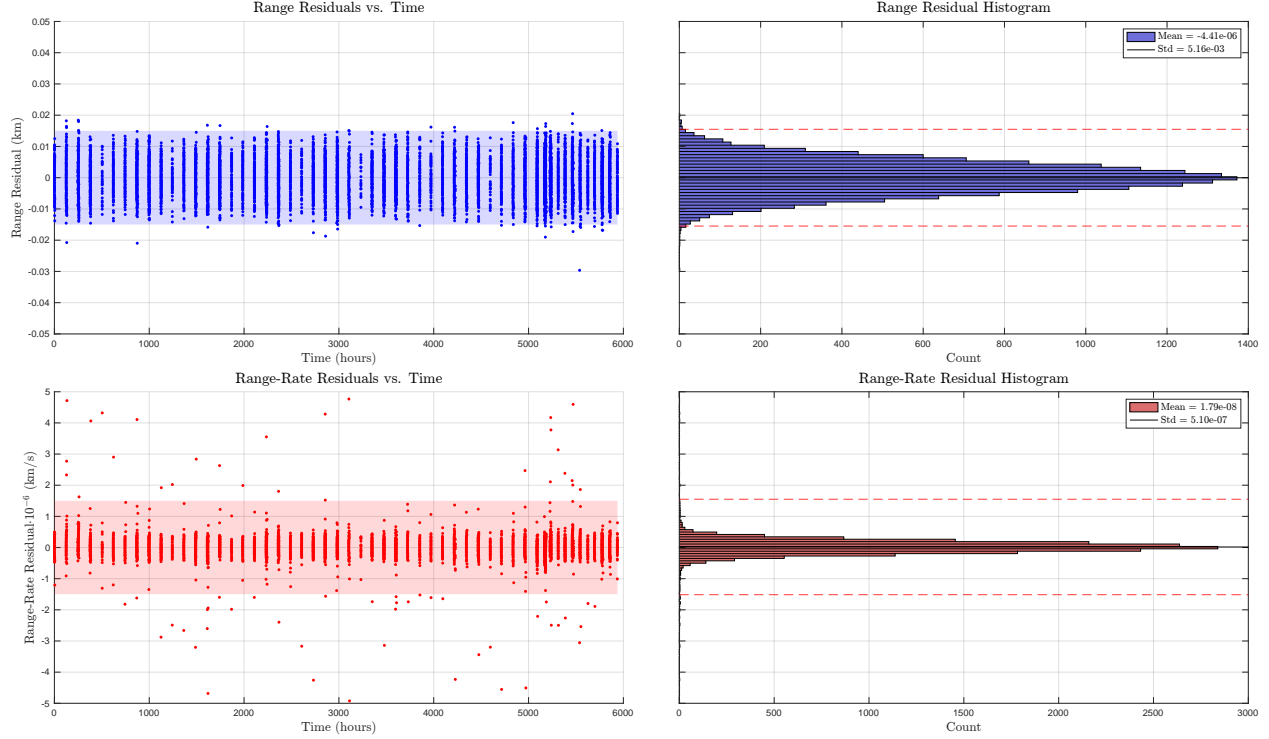


Figure 18: Post-fit residuals for range and range-rate measurements (*OD02*).

4.3.3 *OD01*: LKF+RTS Filtering with DMC and Maneuver Modeling

In this configuration, the primary maneuver is explicitly modeled within the filter, while DMC is employed to absorb residual unmodeled accelerations, simultaneously enabling the explicit estimation of their time-varying profiles. This hybrid approach improves upon previous solutions by capturing both impulsive and continuous dynamical mismodeling. Estimation is again performed using a two-iteration LKF followed by RTS smoothing. The estimated state vector is defined as $[\mathbf{r}, \mathbf{v}, C_R, \Delta\mathbf{v}, t_b, \mathbf{w}]^\top$.

The continuous-time process noise spectral density for the DMC component is set to $q_w = 10^{-11} \text{ km}^2/\text{s}^6$, a typical value for spacecraft stochastic accelerations. The impulsive maneuver vector $\Delta\mathbf{v}$ is initialized at zero, with the maneuver epoch fixed at 5200 hours into the arc. The initial uncertainty on the components of $\Delta\mathbf{v}$ is 10^{-4} km/s , and the a priori uncertainty on the maneuver epoch t_b is set to 10^3 seconds. Empirical accelerations are initialized at zero with an a priori sigma of 10^{-9} km/s^2 . Table 2 summarizes the estimated maneuver parameters, which show consistent signs and magnitudes with the previous solution. A formal Mahalanobis distance check is omitted for brevity.

For this case, a DMC decorrelation time constant of $\tau_i = 10$ days is selected. Although a value of 60 days is found to be optimal in *OD03*, a shorter τ is preferred here to prevent DMC from absorbing the impulsive dynamics of the maneuver. Larger τ values tend to yield nearly constant empirical accelerations that could inadvertently model the maneuver itself. A shorter decorrelation time ensures that the filter distinguishes between the maneuver and stochastic accelerations, allowing the maneuver parameters to assume their appropriate share of the uncertainty. This behavior is confirmed by Figure 21, where the empirical accelerations significantly decrease after the maneuver epoch, indicating that the filter ceased estimating them once the maneuver is performed. Prior to the burn, the empirical acceleration behavior is similar to *OD03*, despite the different τ . Although

further refinement—such as different q_w values before and after the maneuver, or a segmented filtering approach—could improve performance, this solution already achieves near-optimal results.

The time evolution of the $3 - \sigma$ covariance bounds for all estimated states is shown in Figure 19. Uncertainty levels are comparable to *OD02* and *OD03*, consistent with the applied process noise settings. As in previous cases, the maneuver epoch t_b remains poorly observable. Notably, the uncertainty associated with the empirical accelerations decreases significantly after the maneuver, confirming that their contribution is partially absorbed by the now-estimated maneuver parameters.

Post-fit residuals for range and range-rate measurements are shown in Figure 20. Both residual sets are well bounded within the $3 - \sigma$ noise envelope and exhibit white noise characteristics. Only minor outliers are present in the range residuals after the maneuver, with no indication of unmodeled dynamics. While a nonlinear pre-fit residual analysis could—and in principle should—be performed, its interpretability would be limited in the absence of DMC, as modeling discrepancies would persist uncorrected and bias the residual structure.

The reduced chi-squared statistic for this solution is $\chi^2_\nu = 1.0770$, a value that aligns well with the qualitative fit quality. This solution represents a near-optimal trade-off, effectively capturing both the impulsive maneuver and the residual dynamical mismodeling through explicit estimation. Further improvement would require suppressing DMC and relying on improved physical modeling for full predictive capability; however, within the scope and timeline of this analysis, *OD01* provides the most accurate and stable estimation performance.

Table 2: Estimated Maneuver Parameters and $1-\sigma$ Uncertainties (*OD01*)

Parameter	Estimated Value	$\pm 1\sigma$	Units
Δv_x	2.6085×10^{-5}	7.6047×10^{-7}	km/s
Δv_y	-7.6740×10^{-4}	3.0917×10^{-6}	km/s
Δv_z	6.6726×10^{-4}	6.3617×10^{-6}	km/s
t_b	5200.00	0.2778	hr

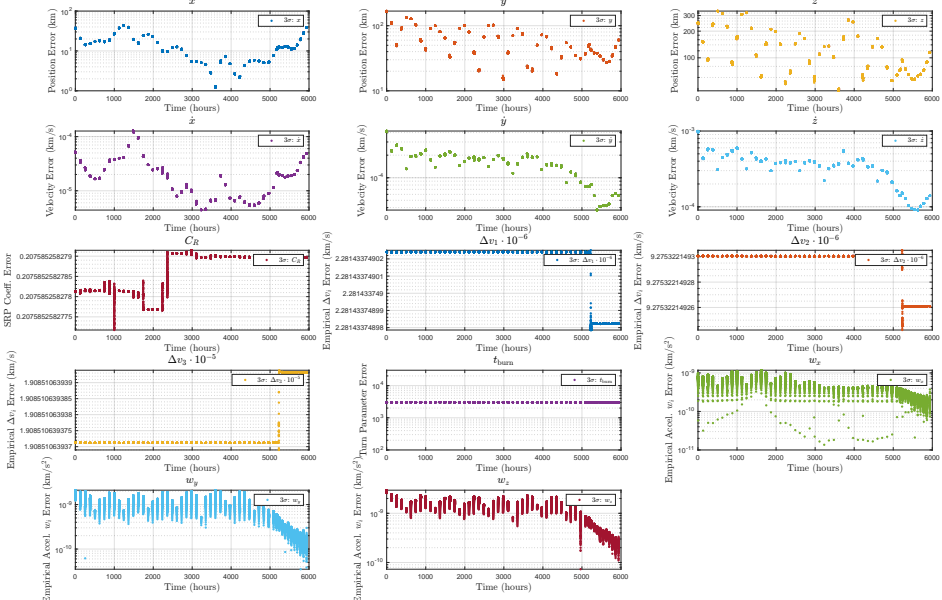


Figure 19: Covariance bounds for *OD01*.

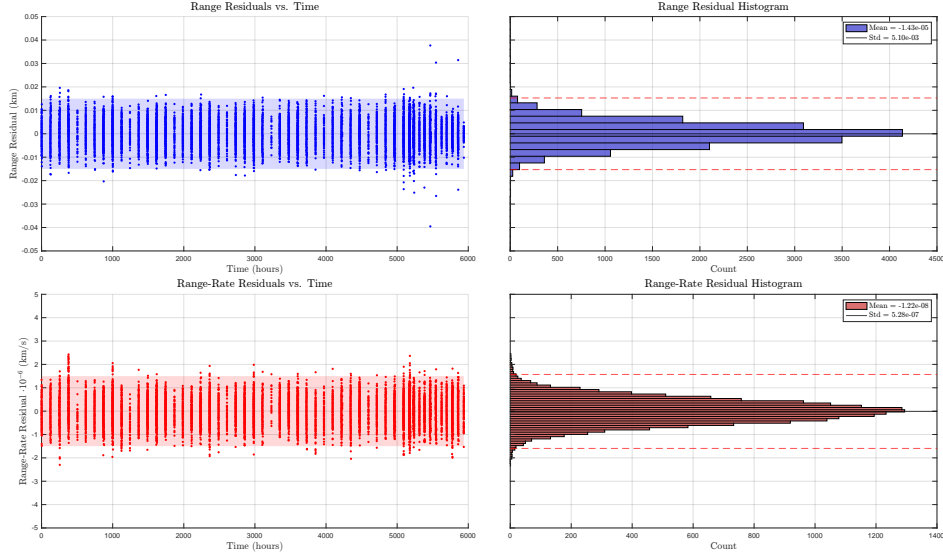


Figure 20: Post-fit residuals for *OD01*.

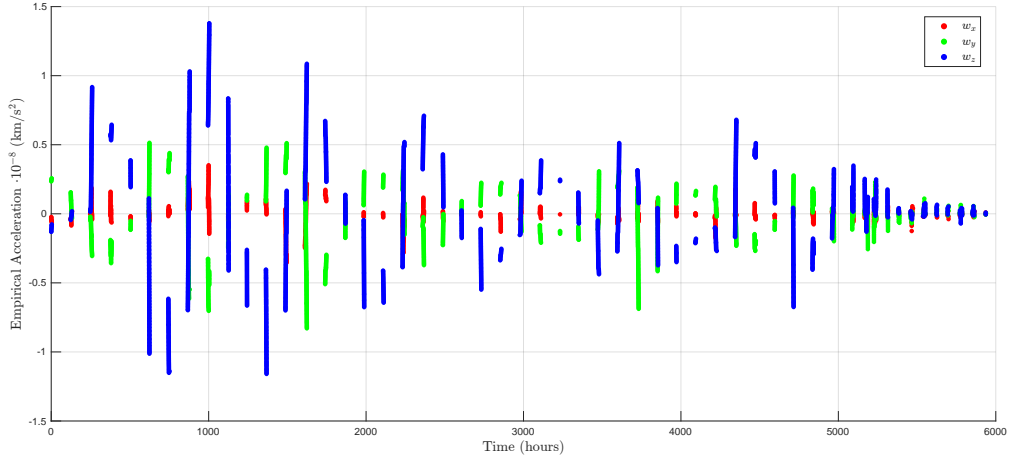


Figure 21: Estimated empirical accelerations during *OD01*.

4.3.4 *OD04*: SRIF Filtering with SNC and Maneuver Modeling

Due to the absence of an SRIF-based smoother and the inability to incorporate correlated process noise within the SRIF framework—primarily owing to time constraints on additional code development—*OD02* serves as the sole reference solution against which consistency is assessed when switching filtering schemes. Since SRIF is fundamentally a numerically stable reformulation of the LKF, the resulting state estimate at the B-plane intersection is expected to closely match that obtained from *OD02*. A smoother is neither applied nor required in this case, as the comparison is conducted at the B-plane, which lies beyond the final epoch t_f —that is, after the last measurement update—where both filtering approaches are expected to yield equally conditioned estimates. All tuning parameters are kept identical to those used in *OD02*.

Covariance envelopes and post-fit residuals are not shown here, as they exhibit the expected behavior: uncertainty levels consistent with sequential filtering (and thus larger than smoothed *OD02* estimates), and residuals bounded within the $3 - \sigma$ envelope. The consistency evaluation is

instead deferred to the B-plane mapping, where final predicted state statistics are directly compared.

4.3.5 OD05: LKF+RTS Filtering with DMC on 100% of the Arc

This configuration replicates the setup of *OD03* but applies DMC over the entire dataset, including the maneuver. The objective is to demonstrate that relying solely on DMC to absorb the effects of an unmodeled impulsive maneuver is insufficient in practice. Although DMC can, in theory, accommodate a $\Delta\mathbf{v}$, it is not suited for capturing the magnitude and precise timing of the maneuver. Moreover, tuning the filter parameters becomes significantly more challenging, often resulting in degraded estimation performance.

All filter settings and parameters are identical to those in *OD03*; the only change is the use of the full arc duration. The post-fit residuals for this case are shown in Figure 22, clearly illustrating the filter's inability to handle the maneuver, with a marked degradation in residual behavior. The maneuver is also reflected in the empirical acceleration estimates shown in Figure 23, where the DMC component temporarily spikes to absorb the abrupt dynamical discontinuity.

This solution is included for completeness. Due to its poor performance and lack of consistency with the other solutions, it is excluded from the B-plane mapping analysis.

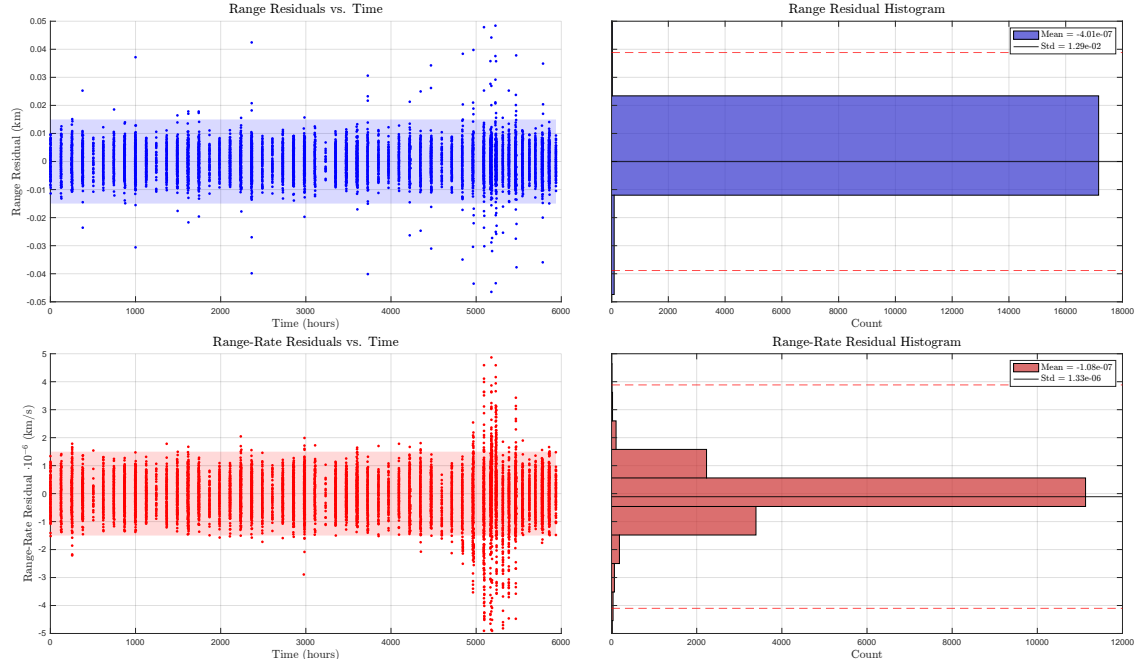


Figure 22: Post-fit residuals for range and range-rate measurements (*OD05*).

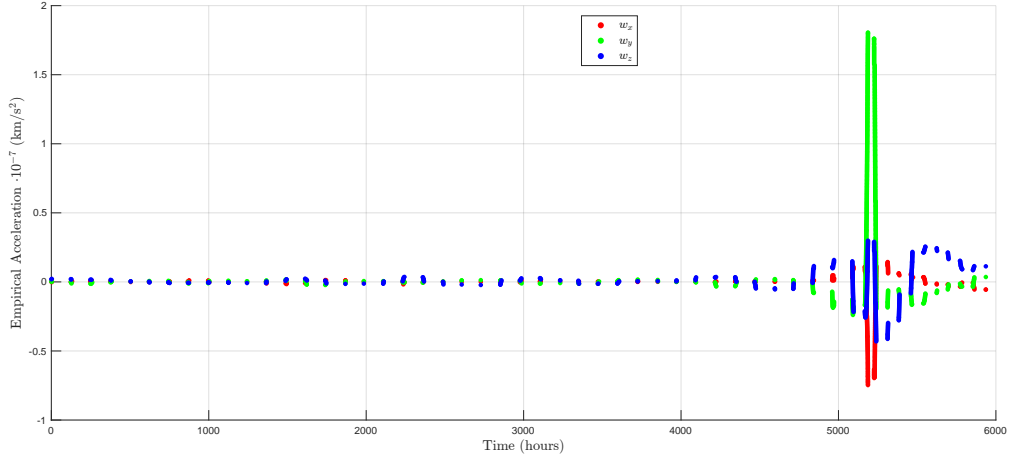


Figure 23: Estimated empirical accelerations showing maneuver absorption (*OD05*).

4.4 Selection of Final Solution

Among the candidate solutions, those lacking explicit $\Delta\mathbf{v}$ estimation are excluded—namely, *OD03*, which does not account for the dataset portion after the maneuver and therefore fails to capture the correct final velocity (resulting in poor B-plane prediction performance), and *OD05*, which also exhibits poor post-fit residuals.

Of the remaining candidates, all of which incorporate maneuver estimation, the solution denoted *OD01*—based on a hybrid approach employing DMC for low-frequency unmodeled dynamics and impulsive $\Delta\mathbf{v}$ estimation for localized burn event modeling—exhibited the most favorable overall performance. This solution demonstrated both excellent visual alignment in residuals and a reduced chi-squared value close to unity. In contrast, *OD02* and *OD04*, although exhibiting favorable chi-squared values, showed degraded performance in terms of range-rate residuals. Additionally, *OD04* did not include smoothing, and thus the epoch estimate is conditioned on only a single measurement.

Based on both quantitative metrics and qualitative behavior, *OD01* is selected as the nominal final solution, using a LKF with a RTS smoother. The estimated state at epoch t_0 is reported in Table 3, while the corresponding B-plane solution is shown in Table 4. All B-plane solutions are plotted in Figure 24; *OD05* is excluded due to its major inconsistency with the others.

Before presenting the B-plane solution in detail, it is important to reiterate a few key points:

1. The use of DMC or SNC in a scenario with substantial unmodeled dynamics (e.g., 10^{-9} km/s² level) can be problematic for prediction tasks. While *OD01* fits the data well, the propagated solution—such as the B-plane intersection—may be biased due to these unmodeled accelerations. Consequently, the resulting B-plane prediction should be interpreted with caution, despite the underlying OD solution being well-constructed.
2. Solutions are assessed primarily using linearized post-fit residuals, rather than full nonlinear residual analysis. While not ideal, this approach is reasonable given the dominance of unmodeled dynamics, which would otherwise skew nonlinear residual interpretation with persistent biases.
3. In an operational OD scenario, further validation would be required. Consistency checks should be performed to assess solution robustness, such as:
 - Estimating solutions using subsets of the data (e.g., Doppler-only, range-only, reduced measurement arcs),

- Running overlapping solutions and checking mutual consistency,
- Evaluating Mahalanobis distances between estimates,
- Verifying prediction envelopes against independent estimates.

These practices are critical to ensuring statistical consistency between solutions.

4. Linearized filters, such as the LKF and SRIF, are known to underestimate the state covariance, especially when compared to nonlinear alternatives like the Unscented Kalman Filter (UKF). To improve the realism of the estimated uncertainty, Consider Covariance Analysis (CCA) should be performed. In this study, however, CCA is omitted due to time constraints.

Despite these caveats, *OD01* provides an excellent fit in terms of post-fit residuals and statistical metrics. It would, however, suffer in prediction contexts if unmodeled dynamics are not properly accounted for. One possible extension would involve parameterizing the DMC empirical accelerations using time-dependent functions (e.g., polynomials or harmonics), although that remains outside the scope of this study.

Regarding the B-plane comparison, *OD03* shows the largest covariance ellipse due to its limited observation arc, highlighting the importance of sufficient measurement coverage. However, its broad uncertainty region conveniently overlaps with more refined solutions, offering indirect confirmation of consistency. *OD02* and *OD04*, which use similar models and differ only in the mathematical form of the filter (LKF vs. SRIF), produce nearly identical results—an encouraging outcome that increases confidence in their validity. *OD01* exhibits a slightly broader uncertainty, and its B-plane solution does not overlap with *OD02*/*OD04* due to its fundamentally different assumptions and inclusion of DMC. Nevertheless, it offers a strong compromise between quantitative and qualitative diagnostics. The increased covariance may also help compensate for the absence of CCA.

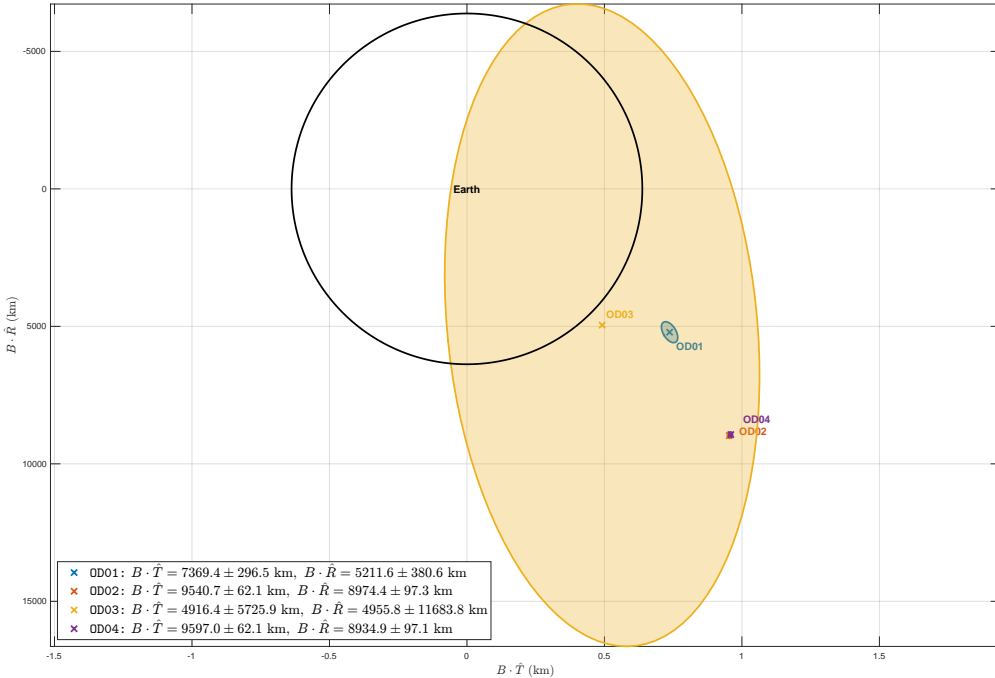


Figure 24: Estimated B-plane Mappings for Problem 3 solutions.

Parameter	Estimate (km)	1- σ Uncertainty (km)
x (km)	-274097792.7126	12.5092
y (km)	-92856901.3998	55.9047
z (km)	-40198035.3279	83.0798
v_x (km/s)	+32.6710	1.7358×10^{-5}
v_y (km/s)	-8.9378	1.3995×10^{-4}
v_z (km/s)	-3.8815	3.3243×10^{-4}

Table 3: Estimated ECI position and velocity at epoch t_0 for *OD01*.

Parameter	Estimate (km)	1- σ Uncertainty (km)
$\mathbf{B} \cdot \hat{\mathbf{T}}$	7369.4206	296.4918
$\mathbf{B} \cdot \hat{\mathbf{R}}$	5211.5514	380.5769
Correlation $\rho(\mathbf{B} \cdot \hat{\mathbf{T}}, \mathbf{B} \cdot \hat{\mathbf{R}})$	0.5007	

Table 4: B-plane Target Estimates, 1- σ Uncertainties, and Correlation for *OD01*.

5 Additional Analysis

Within the scope of the additional analysis, the investigation of the estimated empirical accelerations—conducted in the context of *OD03* solution—has already been completed and stands as the most thorough. The following section presents a set of complementary, though less in-depth, considerations.

5.1 Comparison with Alternative Filters

This study evaluates several OD filters, including the Batch SRIF, the LKF with RTS smoothing, and the sequential SRIF. These filters differ in mathematical formulation, numerical properties, and applicability depending on the estimation context.

Batch filters estimate the state at the reference epoch by conditioning on the entire measurement arc simultaneously. This global formulation is generally preferred—requiring no smoother, as it inherently yields the best estimate—when both the dynamical and measurement models are well characterized. Batch filters do not natively support process noise modeling, which limits their applicability in scenarios involving significant dynamical mismodeling.

Sequential filters, such as the LKF, update the state estimate recursively as new measurements become available. When paired with RTS smoothing, the method recovers the benefits of global conditioning while retaining the flexibility to incorporate time-varying process noise. However, the sequential formulation requires more careful tuning and may suffer from numerical instability. The SRIF addresses this limitation by reformulating the Kalman filter to operate on the square root of the information matrix, significantly improving numerical robustness.

In this project, the batch SRIF is applied in Problem 2 to establish a reference solution under idealized modeling assumptions. For Problem 3, the LKF+RTS framework is adopted as the primary estimator, offering flexibility to accommodate process noise. A sequential SRIF is also employed as a consistency check against the LKF-based solutions. Among the tested approaches, the LKF+RTS configuration strikes the best balance between estimation accuracy and modeling

adaptability. A pseudo-epoch SRIF with stochastic process modeling—effectively a batched DMC implementation—would provide the most rigorous estimation architecture, though it is not implemented here due to time constraints.

5.2 B-plane Sensitivity to Mapping Radius

To assess the sensitivity of the B-plane target parameters to the choice of mapping radius, the event radius r^* used to terminate propagation—at which the spacecraft state is extracted to define the B-plane reference frame—is systematically varied. The mapping radius is defined as a multiple of Earth’s sphere of influence (SOI) radius R_{SOI} , such that

$$r^* = \gamma \cdot R_{SOI}, \quad \gamma \in [0.1, 20.0].$$

For each value of γ , the best estimated trajectory (in this example, corresponding to *OD02*) is propagated forward in time from the final estimation epoch until the spacecraft reached the corresponding r^* . The B-plane coordinates are then computed from the resulting position and velocity vectors. The B-vector is defined as

$$\mathbf{B} = \mathbf{r} - \frac{\mathbf{r} \cdot \mathbf{v}}{\|\mathbf{v}\|^2} \mathbf{v},$$

and projected into the B-plane frame constructed from the orthonormal basis:

$$\hat{\mathbf{S}} = \frac{\mathbf{v}}{\|\mathbf{v}\|}, \quad \hat{\mathbf{T}} = \frac{\hat{\mathbf{S}} \times \hat{\mathbf{z}}}{\|\hat{\mathbf{S}} \times \hat{\mathbf{z}}\|}, \quad \hat{\mathbf{R}} = \hat{\mathbf{S}} \times \hat{\mathbf{T}}.$$

As shown in Figure 25, the B-plane coordinates vary significantly with the selected mapping radius.

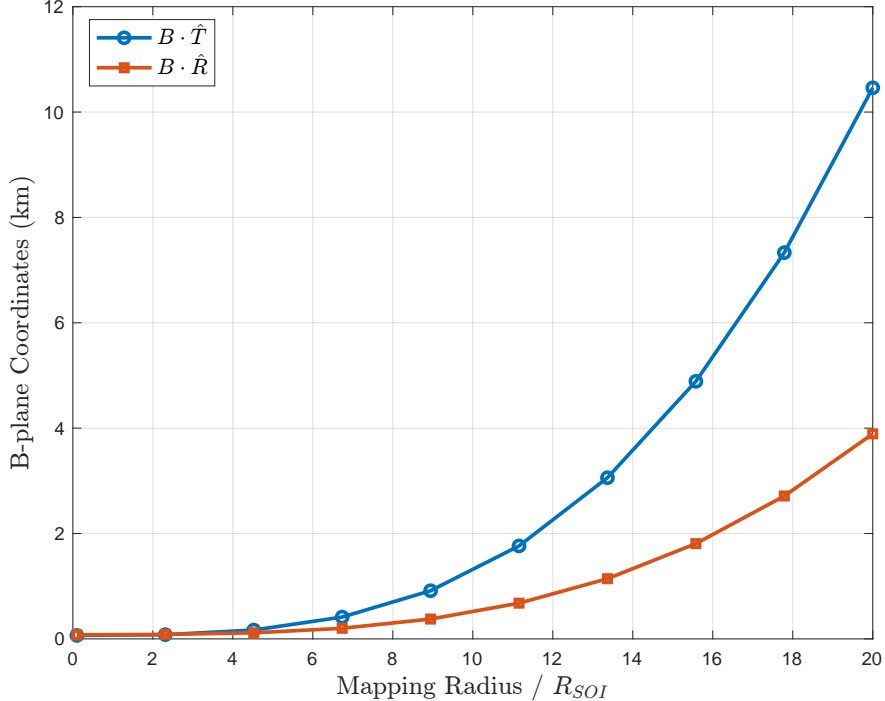


Figure 25: B-plane coordinates $\mathbf{B} \cdot \hat{\mathbf{T}}$ and $\mathbf{B} \cdot \hat{\mathbf{R}}$ as a function of mapping radius, expressed in units of R_{SOI} .

The trend is strictly monotonic, with both $\mathbf{B} \cdot \hat{\mathbf{T}}$ and $\mathbf{B} \cdot \hat{\mathbf{R}}$ increasing as γ increases over the plotted

range. These results highlight the importance of using a consistent and carefully selected mapping radius, particularly in the context of mission operations involving multiple navigation teams or tools. The geometric projection used to compute the B-vector depends on both the position and the orientation of the velocity vector at the mapping point. Consequently, even moderate changes in the propagation endpoint can result in large differences in B-plane coordinates. In the analyzed case, and solely for completeness, varying γ from 0.1 to 20 results in B-vector shifts on the order of 10^5 km.

5.3 Lessons Learned for Real-World Orbit Determination

This project reinforced several practical lessons relevant to real-world orbit determination, particularly when working with imperfect models.

One important takeaway is the benefit of prioritizing high-fidelity force models over relying on complex filtering techniques to compensate for model deficiencies. I once heard Jeff Parker (CTO at Advanced Space) mention—probably quoting George Born (Distinguished Professor and founder of the Colorado Center for Astrodynamics Research at CU Boulder)—that “the best OD is achieved with the most accurate force model and the fewest estimated parameters.” Although observability isn’t a major issue in this study, the principle still holds: estimating fewer parameters helps preserve information content.

This work showed that using empirical accelerations to absorb model mismatches often leads to inflated uncertainties and poor predictive performance. While helpful when models are incomplete, these terms can end up masking missing physics rather than correcting it. In practice, it’s better to directly model known effects—like ray-traced SRP in OSIRIS-REx—than to rely on tuning empirical terms. At the end of the day, the accuracy of the OD solution depends more on the fidelity of the underlying model than on the complexity of the filter.

5.4 Ephemeris Errors

Although not explicitly included in the final results due to poor performance, one of the tests conducted in this study involved the co-estimation of the solar ephemeris by augmenting the state vector with the Sun’s position \mathbf{r}_\odot and velocity \mathbf{v}_\odot . The idea is that deviations from the reference ephemeris can be estimated alongside the spacecraft state if partial derivatives (sensitivities) of the dynamics and measurements with respect to these ephemeris terms are properly modeled.

In general, co-estimation of ephemerides is most effective when the equations of motion are formulated with the subject body at the origin, as this introduces direct sensitivity to ephemeris errors in both the dynamics and the measurement model. In this project, however—as is often the case—the dynamics are Earth-centered, and the Sun (being the perturber of interest) appears only as a third-body force and as the direction for SRP. Consequently, deviations in the Sun’s ephemeris affect the trajectory indirectly, primarily through modifications to the Sun-relative acceleration terms. To simulate this effect, the Sun’s position is modeled as the negative of Earth’s state around the Sun, propagated with a simple two-body model. While this is a coarse approximation compared to full SPICE-based ephemerides, it captures the dominant behavior for sensitivity analysis. This formulation supports two estimation strategies:

- Co-estimation: Ephemeris deviations are included in the estimated state and updated by the filter. However, this might lead to high correlations and poor numerical conditioning.
- Consider Covariance Analysis (CCA): when dealing with well-known ephemerides, a more appropriate approach is to treat their uncertainty as a consider parameter. This involves

propagating the effect of ephemeris errors through the sensitivity matrix \mathbf{S} , allowing their contribution to be reflected in the total state uncertainty without explicitly estimating weakly observable parameters. The total covariance becomes:

$$\mathbf{P}_{\mathbf{c},k} = \mathbf{P}_{\mathbf{x},k} + \mathbf{S}_k \mathbf{P}_{\mathbf{c,c}} \mathbf{S}_k^\top, \quad (1)$$

where $\mathbf{P}_{\mathbf{x},k}$ is the estimated covariance of the state vector, $\mathbf{P}_{\mathbf{c,c}}$ is the a priori covariance of the consider parameters (e.g., ephemeris errors), and \mathbf{S}_k is the sensitivity matrix of the state with respect to those parameters.

In missions to small bodies, where ephemerides may be poorly known, co-estimation becomes necessary. Optical navigation (OpNav) data can significantly enhance observability, enabling joint estimation of both the spacecraft and the target's ephemeris. In contrast, when the ephemeris is highly accurate—as is the case with the Sun—consider covariance is the more robust choice. Ultimately, this section reinforces the importance of balancing model complexity with the sensitivity of the available data.